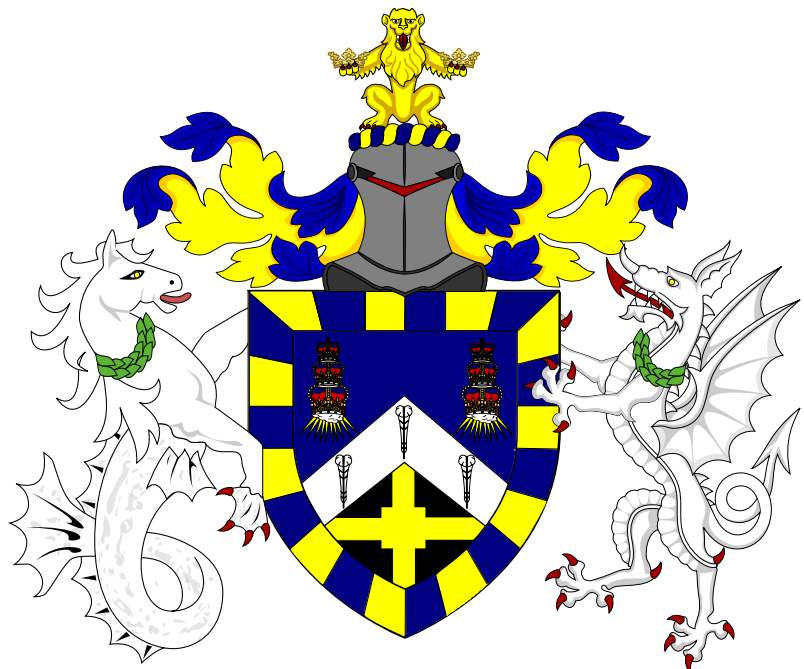


Measurements of $H \rightarrow b\bar{b}$ decays and VH production

Thomas Charman

Supervisor: Dr. Jonathan Hays



Queen Mary University of London

Submitted in partial fulfillment of the requirements of the Degree of
Doctor of Philosophy January 18, 2021.

Contents

1	Introduction	5
2	Physics Theory	7
2.1	Historical Aside	11
2.2	Quantum Electrodynamics	12
2.3	Quantum Chromodynamics	14
2.4	Electroweak theory	15
2.5	The Brout-Englert-Higgs Mechanism	17
2.6	Higgs bosons at the LHC	19
3	The ATLAS Detector at the Large Hadron Collider	21
3.1	The Large Hadron Collider	21
3.2	The ATLAS Detector	26
	Tracking: The Inner Detector	28
	Pixel Detectors	31
	Semiconductor Tracker	31
	Transition Radiation Tracker	33
	Calorimeters	33
	Electromagnetic Calorimeter	35
	Hadronic Calorimeter	35
	Muon Spectrometers	36
	Trigger Systems	37
4	Machine Learning Theory	39

CONTENTS	3
4.1 Boosted Decision Trees	39
4.2 Neural Networks	39
4.3 Parametrised Neural Networks	39
5 Reconstruction and Selection	41
5.1 Triggers	41
5.2 Athena and the CxAOD Framework	41
5.3 Channel Definitions and Lepton Selections	44
5.4 Triggers	44
5.5 Jets	45
5.6 Overlap Removal	45
5.7 Missing Transverse Momentum	45
5.8 Categorisation into Analysis Regions	45
Top $e\mu$ control region	45
$\Delta R(b,b)$ Control Regions	45
6 Fit Models	46
6.1 Profile Likelihood Fits	46
6.2 VH(b,b) multi-variate discriminant fit	46
6.3 Di-jet mass fit	46
6.4 VZ Cross-check fit	46
7 Background Modelling	48
7.1 Novel Modelling Techniques	48
Multi-dimensional re-weighting	48
Inferring missing information with parametrised neural networks . .	48
7.2 2 lepton channel Z + jets modelling	48
Extrapolation to 0 lepton channel	48
7.3 Modelling of other backgrounds	48
8 Results	49
8.1 VH(b,b) multi-variate discriminant fit results	49

<i>CONTENTS</i>	4
8.2 Di-jet mass fit results	49
8.3 VZ Cross-check results	49
9 Conclusion	50
9.1 Future studies	50
Bibliography	51

Chapter 1

Introduction

In 2012 the Higgs boson was discovered by the ATLAS and CMS collaborations at the Large Hadron Collider [1, 2]. It was said to form the last piece of the Standard Model of Particle Physics, a framework that describes three of the four fundamental forces of nature, described in more detail in Chapter 2. Despite apparent completeness after the Higgs discovery, it is known that the theory does not describe gravity, the fourth of the known fundamental forces of nature. The theory also has other shortcomings, it cannot explain the presence of dark matter [3–13] or a number of other observed phenomena [14–18]. So far the model has stood up to all experimental tests [19, 20] concerning its own predictions but there are still parameters of the model that have not been measured. Given the theory’s understood shortcomings, it is hoped that continued scrutiny of the models predictions will yield unexpected results, perhaps hinting at a new way forwards in terms of a theory that describes everything or simply exposing further gaps in our knowledge of the universe. For this reason it is more important than ever to study in detail the most recently discovered piece of the model, the Higgs boson.

This work focuses on studying a specific production mechanism and decay mode of the Higgs boson, specifically a vector boson associated Higgs boson decaying to two bottom quarks, denoted $VH(bb)$. This decay mode is of importance as it is currently the only decay mode of the Higgs decaying to quarks that has been observed [21]. A summary of the full spectrum of production mechanisms and decay modes of the

Higgs will be given in Chapter 2.

The study of this decay mode was carried out with the ATLAS detector, and made possible by the hard work of all members of the ATLAS collaboration. In Chapter 3 the detector is described in full.

Chapter 2

Physics Theory

The following chapter outlines the physics theory that informs and guides the experimental process of searching for new particles or making measurements at a particle collider. Not only are the physics theories described here useful in that context but they also provide an almost complete picture of the universe at certain scales. This chapter was written with the aid of notes taken at the annual STFC High Energy Physics Summer School, and with the aid of several books [22, 23], in which a more detailed description of the theories can be found.

The Standard Model of particle physics is a theoretical framework that describes all elementary particles and three of the fundamental forces of nature. Notably the only force that is not described by the theory is gravity. Particles described by the model are listed in table 2.1 with a white gap separating the matter particles (fermions) from the force carrying particles (bosons). Fermions, which make up solid matter obey Fermi-Dirac statistics [24, 25] whereas bosons obey Bose-Einstein statistics [26]. The Higgs boson is special in that as far as we know it does not carry a force in the conventional sense, instead it is responsible for giving fundamental particles mass, discussed in more detail in section 2.5. In the table of particles quarks (blue) and leptons (red) are ordered in columns by increasing mass, apart from the neutrinos, which are massless in the theory.

As mentioned the model describes forces as being mediated by certain particles, the photon (γ) mediates the electromagnetic force, particles experiencing electro-

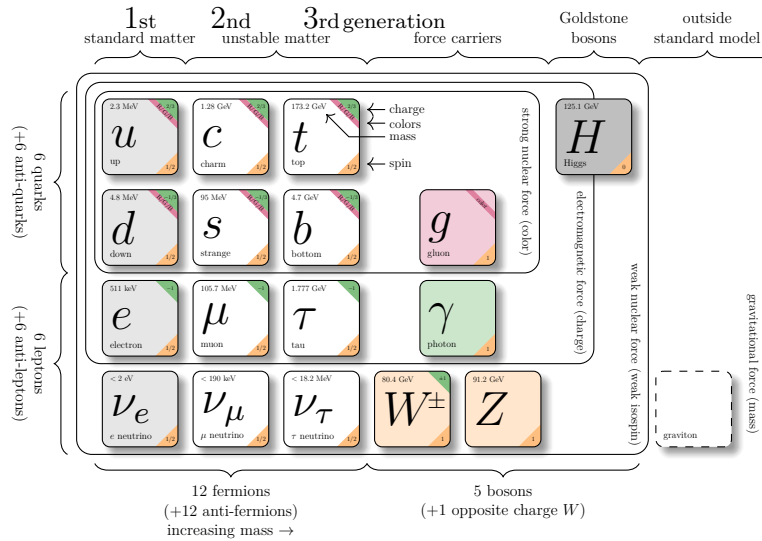


Table 2.1: The particles of the standard model with fermions displayed on the left and bosons on the right. Quarks are in blue, leptons in red, vector bosons in yellow and scalar bosons in green.

magnetic repulsion or attraction are described as exchanging photons. The strength and direction of the force experienced is proportional to the electromagnetic charge of particles involved. The Standard Model is a theory of quantum fields in which the strength of interactions between fields, or particles which are described as excitations in the fields, is parametrised by something known as a coupling constant. It is natural to assume that the strength of the interaction between photons and charged particles is related to the electromagnetic charge of the particles involved. Indeed this is the case consider the Coulomb force between two protons,

$$F = \frac{e^2}{4\pi\epsilon_0 r}, \quad (2.1)$$

where e is the elementary charge, ϵ_0 is the electric constant and r is the distance between the two protons in question and also the energy of a photon given by

$$E = \frac{hc}{\lambda}, \quad (2.2)$$

where h is Planck's constant, c is the speed of light and λ is the wavelength of the

photon. The value of the ratio of these two quantities

$$\alpha = \frac{e^2 \lambda}{4\pi\epsilon_0 r hc}, \quad (2.3)$$

known as the fine structure constant, is the coupling constant that describes the strength of the interactions between the photon field and fields of particles with electromagnetic charge. So as is now clear this coupling constant does indeed depend on the electromagnetic charge of the objects involved and so it is not in fact constant.

As well as the electromagnetic force the Standard Model describes the strong nuclear force and the weak nuclear force, shortened to just the strong and weak forces respectively. Like the electromagnetic force they too are mediated by the exchange of particles, the gluons (g) carry the strong force and the W^\pm and Z^0 bosons carry the weak force.

The charge associated with the strong force is known as colour which can take values that are mapped onto colours in the visible spectrum (red, green, blue) for ease of description. For each of these colours an anti-colour is also allowed (anti-red, anti-green, anti-blue). Unlike with the electromagnetic charge, particles with colour charge are not found freely in nature. Instead we find particles known as hadrons which are bound states of quarks and anti-quarks (e.g. the proton). The phenomenon of coloured particles being bound in such a manner is known as colour confinement, and the bound states are described by the quantum numbers isospin (I) and hypercharge (Y_c). It is commonly assumed that all free particles in nature are colour singlets e.g. for a hadron the state could be written as

$$\frac{(r\bar{r} + b\bar{b} + g\bar{g})}{\sqrt{3}}, \quad (2.4)$$

where r , b and g represent red, blue and green charges respectively. This phenomenon is known as quark confinement. Gluons carry colour and anti-colour indicating that there should be nine possible quantum mechanical states for the gluon given the available number of colour/anti-colour combinations, however when one

considers that the strong force is exclusively short range, and therefore that there should be no free gluons (disallowing colour singlet gluons) the number of possible states is reduced to eight. The state of a particle, as far as its description with respect to the strong force is concerned, is given by a vector which lives in a vector space, in which elements of the Lie group $SU(3)_C$ act as unitary operators, where the C denotes that the group is associated with the colour charge. The $SU(3)$ group is the group of 3×3 unitary matrices whose determinant is one. These correspond to the eight generators of $SU(3)$ where in general for a group $SU(N)$ the number of generators is given by $N^2 - 1$.

Describing the weak force requires introducing further quantum numbers weak isospin T and weak hypercharge Y_W . The state of a particle with regards to the weak force is given by a vector which lives in a vector space in which elements of $SU(2)_L \times U(1)_{Y_W}$ act as unitary operators where the L denotes that only particles in left-handed chiral states interact with the weak force¹. Left-handed fermions are represented as doublets in the theory with weak isospin $T = 1/2$ whilst right-handed fermions are singlets with weak isospin $T = 0$.

Along the way we have described particle states with respect to particular forces as vectors living in some vector space where the action of the element of a group has been as a unitary operator. If we are to describe a particle state taking into account the full model, the group whose elements should act as unitary operators on the particle state (the gauge group) is $SU(3)_C \times SU(2)_L \times U(1)_{Y_W}$. For each of the groups in the direct product we have established a (gauge) symmetry and therefore due to Noether's theorem [27] there should be an associated conserved quantity. The conserved quantities in this case are the electric charge, the weak hypercharge and isospin and the colour charge.

¹More specifically only left-handed chiral particles participate in weak charged current interactions.

2.1 Historical Aside

This section provides some historical context surrounding the Dirac equation which will later be used as the starting point in the discussion of quantum electrodynamics, which is the sector of the Standard Model that describes electromagnetic interactions.

In 1905 Albert Einstein first proposed the idea of special relativity [28]. The aim of the idea was to unify the then inconsistent theories of Maxwell's electromagnetism and Newtonian mechanics. The result of Einstein's work was a theory of motion which agreed with the predictions of Newtonian mechanics at velocities much smaller than the speed of light but whose predictions were accurate also at much higher velocities (for which Newtonian predictions fail). Arguably, the most far reaching consequence of special relativity is that it demands that any equation of motion must be invariant under Lorentz transformations, at least in terms of the formulation of new theories is concerned. Many physical phenomena predicted by special relativity could be considered of higher consequence in general, for example the phenomena of length contraction, time dilation, energy-mass equivalence and the universal speed limit (equal to the speed of light in vacuum), all of which are extensively scrutinised experimentally [29–35]. It is the Lorentz transformation however that should be kept in mind for the following discussion, the transformation may be written as

$$\begin{aligned} t' &= \gamma(t - vx/c^2) \\ x' &= \gamma(x - vt) \\ \text{with } \gamma &= \frac{1}{\sqrt{1 - v^2/c^2}}, \end{aligned} \tag{2.5}$$

in a single dimension of space x and one of time t where v represents the velocity of the system described by the primed coordinates relative to the unprimed coordinates and c is the speed of light in vacuum.

Twenty years after Einstein introduced the ideas of special relativity Erwin Schrödinger postulated new ideas regarding the motion of quantum mechanical systems [36].

Though he knew his new equation was not invariant under Lorentz transformations, and therefore incomplete, Schrödinger's formulation of quantum mechanics changed the way physicists thought about the universe for ever. His famous equation

$$i\hbar \frac{\partial}{\partial t} \Psi(\vec{x}, t) = \left(\frac{-\hbar^2}{2m} \nabla^2 + V(\vec{x}, t) \right) \Psi(\vec{x}, t), \quad (2.6)$$

describes the states of particles as wave-functions Ψ which can only be interpreted in a probabilistic manner and contains Planck's constant the quantum of action. This work had many consequences including the quantisation of the values of measured observables (meaning they can only take discrete values) and the descriptions of particles as waves.

It was the aim of Paul Dirac to make the Schrödinger equation Lorentz invariant and thus provide a more complete description of quantum systems. Along the way he came to the realisation that in order for his equation to satisfy his needs the wave-function had to be replaced with a four component spinor (ψ) and the introduction of matrices known now as the Dirac matrices (labeled γ^μ with $\mu = 0, 1, 2, 4$) was required. Though not the form he originally wrote down Dirac's Lagrangian density takes the form

$$\mathcal{L}_{Dirac} = \bar{\psi}(i\gamma^\mu \partial_\mu - m)\psi, \quad (2.7)$$

where the repeated up and down indices are implicitly summed over (∂_μ represents the partial derivative taken with respect to a spatial coordinate $\mu = 1, 2, 3$ or time $\mu = 0$).

2.2 Quantum Electrodynamics

In order to take Dirac's Lagrangian (eq. 2.7) and turn it into something that appropriately describes quantum electrodynamics (QED), we should consider a $U(1)$

gauge transformation of the Dirac spinor and it's adjoint

$$\begin{aligned}\psi \rightarrow \psi' &= e^{i\alpha(x)}\psi, \\ \bar{\psi} \rightarrow \bar{\psi}' &= e^{-i\alpha(x)}\bar{\psi},\end{aligned}\tag{2.8}$$

with $\bar{\psi} \equiv \psi^\dagger \gamma^0$ and where $\alpha(x)$ is a local phase. Under this transformation the Lagrangian transforms as

$$\mathcal{L}_{Dirac} \rightarrow \mathcal{L}'_{Dirac} = \bar{\psi}(i\gamma^\mu \partial_\mu - m)\psi - \bar{\psi}\gamma^\mu \alpha(x)\psi\tag{2.9}$$

which is not equivalent to the original due to the factor resulting from the derivative of the transformed spinor. Instead let us change the derivative to the gauge covariant derivative

$$D_\mu = \partial_\mu + ieA_\mu\tag{2.10}$$

where we interpret A_μ as the photon field, with coupling constant e , parametrising the interaction strength. The field is also referred to as the electromagnetic gauge field since it arrives during the process of making the Lagrangian invariant under the $U(1)$ group, the gauge group of electromagnetism. Note that here what we have labeled e is nothing more than the fine structure constant previously denoted α in eq. 2.3. The transformation of the new field under the action of the gauge is defined as

$$A_\mu \rightarrow A'_\mu \equiv A_\mu - \frac{1}{e}\partial_\mu \alpha(x).\tag{2.11}$$

This means that the action of the gauge covariant derivative on the spinor transforms as

$$D_\mu \psi \rightarrow D'_\mu \psi' = e^{i\alpha(x)} D_\mu \psi\tag{2.12}$$

which means that the new Lagrangian

$$\mathcal{L} = \bar{\psi}(i\gamma^\mu D_\mu - m)\psi\tag{2.13}$$

is invariant under the action of the gauge as desired. What remains in order to write a description of QED is to write down a kinetic term for the photon field. An appropriately gauge and Lorentz invariant term is

$$-\frac{1}{4}F_{\mu\nu}F^{\mu\nu} \quad (2.14)$$

where the electromagnetic tensor is defined as

$$F_{\mu\nu} \equiv \partial_\mu A_\nu - \partial_\nu A_\mu. \quad (2.15)$$

Putting everything together we can define the Lagrangian for QED as

$$\mathcal{L}_{QED} = \bar{\psi}(i\gamma^\mu D_\mu - m)\psi - \frac{1}{4}F_{\mu\nu}F^{\mu\nu} \quad (2.16)$$

2.3 Quantum Chromodynamics

Quantum Chromodynamics (QCD) is the theory of the strong force. Its mathematical formulation is similar to that of QED. Except the gauge group for QCD is $SU(3)_C$ where the C denotes that the force is associated with colour charge. As previously discussed the eight generators of the group are associated with the eight gluons of the Standard Model. The generators are present in the form of the transformation of a fermion field under an element of $SU(3)$

$$\psi \rightarrow \psi' = \exp\left(i\alpha_a(x) \cdot \frac{\lambda_a}{2}\right)\psi, \quad (2.17)$$

where the λ_a are the Gell-Mann matrices, generators of $SU(3)$. A key difference between the strong force and the other forces described by the Standard Model is that it increases in strength with range. This property leads to a phenomena known as quark confinement which has been discussed previously. Quark confinement is the reason for many of the complications that arise when trying to detect certain particles in a particle detector such as ATLAS. Specifically, quarks that are produced

in collisions undergo a process called hadronisation whereby they transition from their coloured states to colour singlets. Excess energy present in this process results in the creation of lots of different states, some which decay to leptons, with the overall process producing a conical shower of particles known as a jet.

2.4 Electroweak theory

The Glashow-Salam-Weinberg model of electroweak interactions [37–39] describes the weak force and electromagnetism as a quantum field theory, which is gauge invariant under transformations that are elements of $SU(2)_L \times U(1)_{Y_W}$. As previously mentioned the L and Y_W subscripts denote that the gauge groups in the direct product that are associated with left-handed chiral particles and weak hypercharge respectively. The association with weak hypercharge distinguishes this $U(1)$ group with the $U(1)$ group from QED. The transformation of the fermion fields under $SU(2)$ is given by

$$\psi \rightarrow \psi' = \exp\left(i\vec{\alpha}(x) \cdot \frac{\vec{\sigma}}{2}\right)\psi, \quad (2.18)$$

where $\vec{\sigma}$ is a vector of the Pauli matrices σ_i with $i = 1, 2, 3$, a familiar representation of $SU(2)$ generators. Constructing a gauge covariant derivative for the full transformation under $SU(2) \times U(1)$ requires the addition of new fields analogous to the photon field from QED, the new derivative takes the form

$$D_\mu = \partial_\mu - i\frac{g_1}{2}Y_W B_\mu - i\frac{g_2}{2}\sigma_i W_\mu^i, \quad (2.19)$$

where coupling constants g_1 and g_2 parametrise the strength of interactions with each field. The index i runs over the three Pauli matrices and three new fields W_μ^i with $i = 1, 2, 3$ which are associated with the $SU(2)$ gauge. The B_μ field is associated with the $U(1)_{Y_W}$ gauge and is obtained in the same way as the photon field in QED but is given a new symbol as it is *not* the photon field.

In fact none of the fields added here are the physical fields that we have access to in nature associated with the electromagnetic force or the weak currents. In order

to obtain the physical fields for the weak charged current one can simply take the linear superposition

$$W_\mu^\pm = \frac{1}{\sqrt{2}}(W_\mu^1 \mp iW_\mu^2). \quad (2.20)$$

In order to recover the photon field and reveal the field for the weak neutral current the idea of weak mixing must be introduced. Weak mixing was introduced to theory after the discovery of parity violation [40]. Parity is equivalent to chirality for massless particles, however for particles with mass a Lorentz boost can always appear to flip the chirality of the particles state whereas parity is a fundamental property of a particle. A fermion field with left or right handed chirality can be obtained by multiplication with one of two corresponding projection operators defined as

$$\begin{aligned} P_L &= (1 - \gamma^5)^2/2, \\ P_R &= (1 + \gamma^5)^2/2, \end{aligned} \quad (2.21)$$

with $\gamma^5 = i\gamma^0\gamma^1\gamma^2\gamma^3$, where γ^μ are the Dirac matrices, like so

$$\begin{aligned} \psi_L &= P_L\psi, \\ \psi_R &= P_R\psi. \end{aligned} \quad (2.22)$$

It is known that the weak neutral current and indeed the electromagnetic force both interact with particles of left and right handed chirality. Spontaneous symmetry breaking, theorised to have occurred due to an electroweak phase transition in the early universe, has the effect of rotating the plane defined by the B_μ and W_μ^3 fields into the physical fields we see in nature today. The mixing of the fields due to this rotation takes the form

$$\begin{pmatrix} A_\mu \\ Z_\mu \end{pmatrix} = \begin{pmatrix} \cos \theta_W & \sin \theta_W \\ -\sin \theta_W & \cos \theta_W \end{pmatrix} \begin{pmatrix} B_\mu \\ W_\mu^3 \end{pmatrix}, \quad (2.23)$$

where θ_W the Weinberg angle parametrises the amount of mixing. This picture shows that unification of QED and a description of the weak force has been achieved.

Although it at first seems like the $U(1)_{EM}$ gauge group is not present in $SU(2)_L \times U(1)_{Y_W}$ gauge group of electroweak theory it has been shown that the QED gauge symmetry is recovered by spontaneous symmetry breaking. Also the Y_W subscript in the gauge group represents weak hypercharge which is related to electric charge Q by the following relationship

$$Y_W = 2(Q - T^3), \quad (2.24)$$

where T^3 is the third component of isospin, the component that is conserved.

The particles associated with the weak neutral and charged currents are observed to have masses in nature [41–44] therefore one would naively like to write mass terms of the form

$$\mathcal{L}_{mass} \propto M_B^2 B^\mu B_\mu \quad (2.25)$$

$$+ M_W^2 W_a^\mu W_a^\mu. \quad (2.26)$$

The above mass terms are however not gauge invariant therefore another solution is required, one which will be discussed in the next section.

2.5 The Brout-Englert-Higgs Mechanism

The Brout-Englert-Higgs mechanism was made complete almost simultaneously by R. Brout and F. Englert [45], P. Higgs [46] and, G. Guralnik, C. R. Hagen and T. Kibble [47]. The underlying mechanism was proposed prior to this work by P. Anderson [48], though this initial theory was not relativistic invariant. It was initially proposed as a means to give the vector bosons mass terms that were gauge invariant. The theory predicts a complex scalar field (the Higgs field) that undergoes spontaneous symmetry breaking. Interactions with this field are predicted to be mediated by a massive spin-1 scalar particle that is now known to be the Higgs boson. This particle also gives mass to the fermions via a different mechanism. In

general spontaneous symmetry breaking is a process by which a symmetry breaks once conditions meet some threshold. An example of this is a hot sphere of ferromagnetic material whose spins are isotropically oriented. As the sphere cools the ferromagnetic property of the material will align the spins. In the hot scenario the sphere had symmetry in all spatial directions, by this it is meant that the changes to the sphere's orientation were indistinguishable. Once the spins have aligned however this is no longer the case, the fact that the spins point in a specific direction means that direction is special and so some of the symmetry was spontaneously broken. It can be noted though that a preserved symmetry still exists as rotations about the axis defined by the direction of the spins would leave the sphere invariant. In the Standard Model the symmetry that breaks is that of the complex scalar Higgs field. Consider a Lagrangian involving the field ϕ of the form

$$\mathcal{L} = T - V(\phi) = \partial_\mu \phi^\dagger \partial^\mu \phi - \mu^2 \phi^\dagger \phi + \lambda (\phi^\dagger \phi)^2, \quad (2.27)$$

$$\text{with } \phi = \frac{1}{\sqrt{2}}(\phi_1 + i\phi_2). \quad (2.28)$$

Invariance under global phase transformations of the form $\phi \rightarrow e^{i\theta}\phi$ depends on the parameters of the potential μ and λ . Figure 2.1 shows two sketches of the potential for the scenarios where $\mu^2 > 0$, $\lambda < 0$ (left) and $\mu^2 < 0$, $\lambda < 0$ (right). To suggest

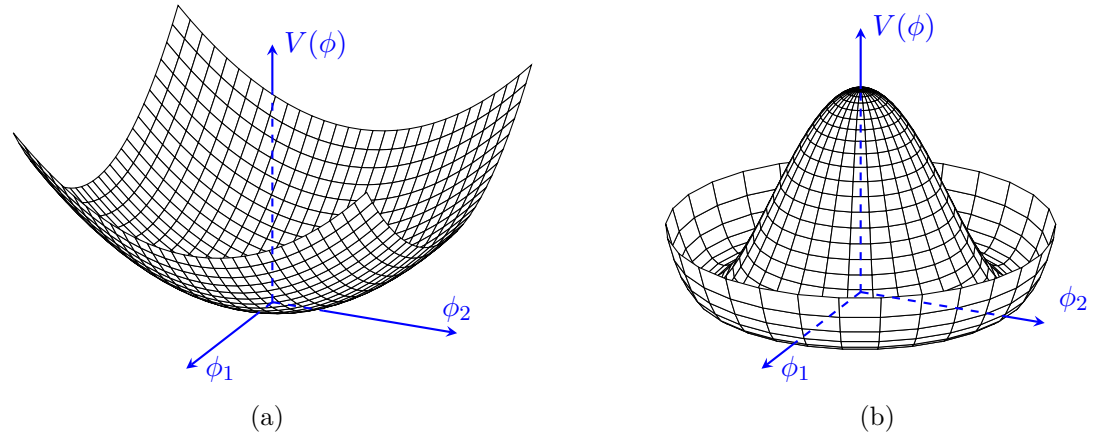


Figure 2.1: The Higgs potential in its fully and broken symmetric forms.

that in our universe this symmetry is spontaneously broken is to suggest that the values of these parameters evolved over time from the full to the broken state. This

ends up leading to masses for the vector bosons that are dependent on μ^2 .

2.6 Higgs bosons at the LHC

Higgs bosons are produced at the LHC in a number of different ways, the four most common of which are shown in figure 2.2. The prevalence of these processes

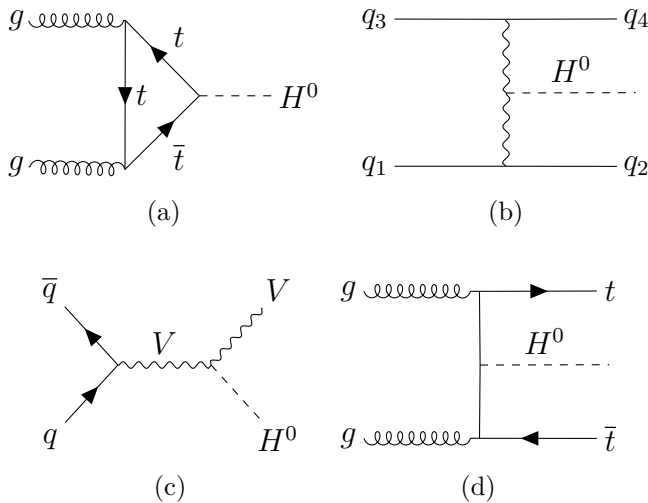


Figure 2.2: The four most common Higgs boson production methods from proton-proton collisions at the LHC.

with respect to the centre of mass energy of the proton-proton collision is shown in figure 2.3 (a). It can be seen the gluon-gluon fusion (fig 2.2 a) is by far the dominate contributor occurring over an order of magnitude more than the next highest process which is quark associated production (fig 2.2 b). The next highest production channel with respect to cross section is vector boson associated (fig 2.2 c) which will be the focus of the rest of this report. Finally top quark associated production (fig 2.2 d) has the smallest cross section of these processes. The Higgs boson is predicted by the Standard Model to decay in a number of different ways depending on its mass, a free parameter of the model. In figure 2.3 (b) the branching ratios of the Higgs can be seen, plotted with respect to Higgs mass. The decay that will be focused on for the rest of this report is $H \rightarrow b\bar{b}$. Given that the focus here is on vector boson associated production of a Higgs boson it is also important to consider the decay of the vector boson. Three possible scenarios are represented in

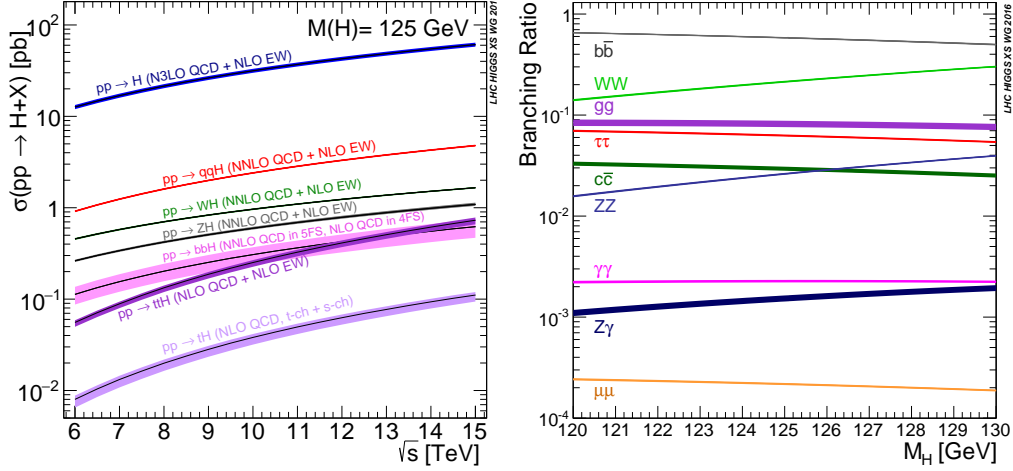


Figure 2.3: Higgs production cross-sections (left), and branching ratios (right) for a range of centre of meass energies and Higgs boson masses respectively [49].

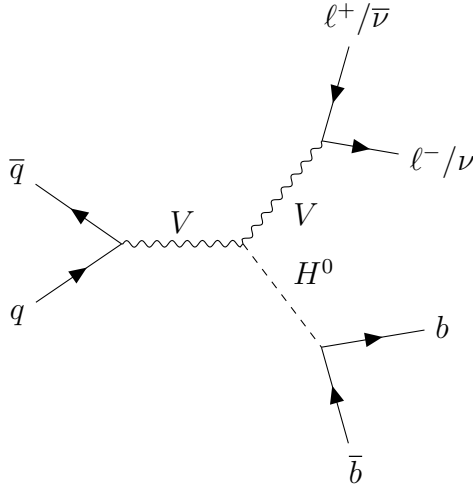


Figure 2.4: A diagram showing a Higgs boson (decaying to a pair of b quarks) produced in association with a vector boson (decaying to 0, 1, or 2 charged leptons denoted $\ell^{+/-}$).

figure 2.4, namely the situations where the vector boson decays to 1, 2 or 3 charged leptons and the appropriate number of neutrinos. It is in fact these leptonic decay modes that motivate the reason for studying this production mechanism as opposed to one of the more common ones. The issue with looking at the other production modes is that very large QCD generated backgrounds are present due to initial state radiation. Whilst these backgrounds are also present when looking at the vector associated channel they can be partially suppressed by triggering on a lepton.

Chapter 3

The ATLAS Detector at the Large Hadron Collider

3.1 The Large Hadron Collider

The Large Hadron Collider (LHC) [50] is a large circular machine located 100 m underground straddling the Swiss-French border at the European Organisation for Nuclear Research (CERN). The LHC accelerates and collides protons and other charged particles. It has a diameter of 27 km and resides in a tunnel which was originally excavated for the Large Electron-Positron Collider [51] experiment. During its construction the tunnel was the largest civil engineering project in Europe to date. Today there are many physics experiments that take place at CERN, some of which are marked in figure 3.1. There are currently seven experiments that record data from the collisions at the LHC: ATLAS [52], CMS [53], LHCb [54], ALICE [55], MoEDAL [56], TOTEM [57] and LHCf [58].

The Lorentz force is fundamental to the LHC's accelerator technologies and detectors. Expressed as

$$\vec{F} = q(\vec{E} + \vec{v} \times \vec{B}), \quad (3.1)$$

it is clear that the force due to an electric field \vec{E} on a particle with charge q acts in the direction of the velocity of the field whereas the force due to a magnetic field \vec{B}

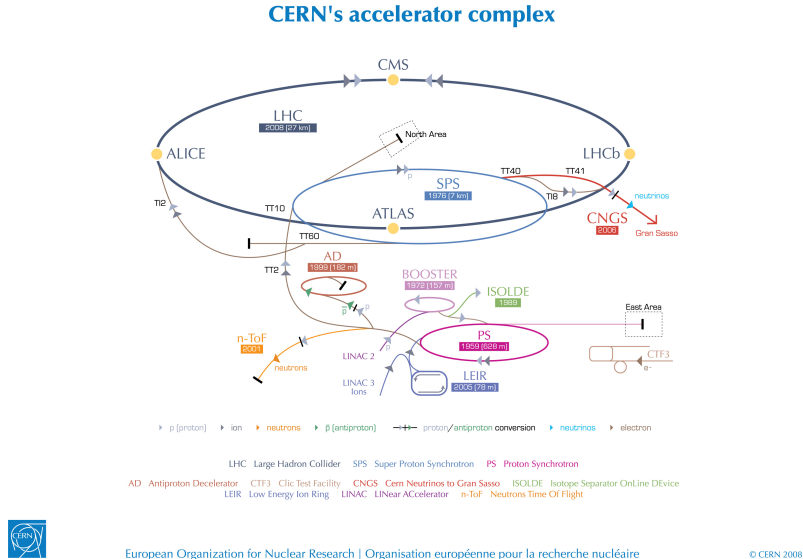


Figure 3.1: The CERN accelerator complex [59].

acts perpendicular to both the field and the velocity of the particle \vec{v} . It is therefore clear that an electric field may be used to accelerate and give energy to a charged particle whereas a magnetic field will alter the trajectory of a particle whilst keeping its energy constant.

The LHC is a synchrotron, an accelerator that uses magnets in a dipole configuration, such as in figure 3.2, to bend the path of charged particles into conformity with its circular shape. It is apparent from studying the figure that counter-rotating beams of same sign charged particles will require two sets of dipole magnets in order to rotate in opposite directions around the same ring. This is one disadvantage of a proton-proton collider with respect to a proton-anti-proton collider such as the Tevatron [60] which can use the same magnets for both beams. On the other hand, the proton-proton collider is able to separate the beams after they have been brought together to collide with a single dipole. The bending magnets of a synchrotron are designed to ramp up their magnetic field in synchronisation with the kinetic energy of the accelerated particles, allowing higher energies to be achieved before the beam is lost. The LHC can accelerate each beam to an energy of 6.5 TeV leading to collisions with a centre of mass energy of $\sqrt{s} = 13$ TeV, although the design energy of the LHC is $\sqrt{s} = 14$ TeV. The Tevatron held the previous record for centre of mass energy of collisions of $\sqrt{s} = 2$ TeV. The LHC has 1232 dipole magnets [50] which

are made of copper-clad niobium-titanium cables, a superconducting material whose electrical resistance falls to zero below 10 K. In order to maintain super-conductivity a cryogenic system using liquid helium is employed to cool the magnets. The higher the velocity of a charged particle, and the tighter the desired bending radius, the larger the magnetic field required to perform the bending. The large size of the LHC and the choice of superconducting magnet technologies are both informed by the aim to accelerate protons to the highest energy, and therefore velocity, possible.

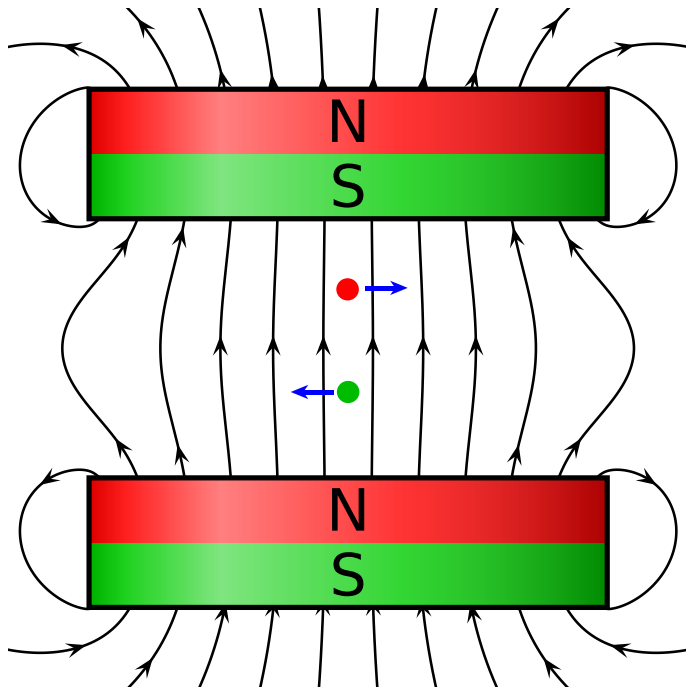


Figure 3.2: A representation of a pair of idealised cylindrical magnets in a dipole configuration. Two positively charged particles are shown as circles, the red particle is traveling out of the page, the green particle is traveling into the page. The forces experienced by each particle due to the magnetic field are shown as blue arrows.

The force which accelerates the particles is provided by radio-frequency cavities such as in figure 3.3, of which the LHC has 16 [50] The electric field in the radio-frequency cavity forms a standing wave, the separation between bunches of particles to be accelerated must be matched to the frequency of this wave. Protons in the LHC are accelerated in bunches and in vacuum, this to increase the likelihood of collisions and mitigate loss of energy and scattering effects due to interactions with air molecules. These two factors lead to the occurrence of space charge which causes

an increase in the emittance of the beam, where the emittance is defined as the total area that the beam occupies in its beam-pipe. The greater the energy of the particles the more they can overcome increase in emittance due to space charge. Increased emittance is especially problematic in circular accelerators where periodic effects can quickly lead to the loss of beam. For these reasons it would be very challenging to accelerate protons from rest in a synchrotron, the starting point for the protons of the LHC is therefore a linear accelerator called Linac2 [?] which is used to overcome space charge effects before the protons move on to a series of synchrotrons as seen in figure ??.

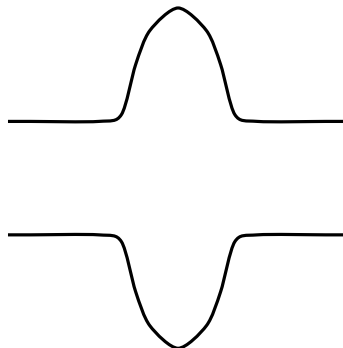


Figure 3.3: A representation of a radio-frequency cavity where the electric field lines are shown in black.

Even a beam with its emittance under control would still be lost from the accelerator if only dipole magnets were used to control its path. Magnets in a quadrupole configuration as in figure 3.4 are used to focus the beam and keep it in the beam-pipe. The quadrupoles behave such that particles feel a force that increases with the distance from the centre of the beam leading to simple harmonic motion of individual particles in a bunch. The LHC has a series of 24 quadrupole magnets each for focusing in the horizontal and vertical directions [50] as well as higher multipolarity configurations; sextupole, octupole, decapole and dodecapole which are used to correct imperfections in the fields of other magnets.

The statistical nature of particle physics analyses means that larger datasets (more recorded collisions) increase the sensitivity of searches and measurements. Constraints on the number of years the LHC is able to run mean that the best way to record more collisions is to collide more particles per second. A quantity

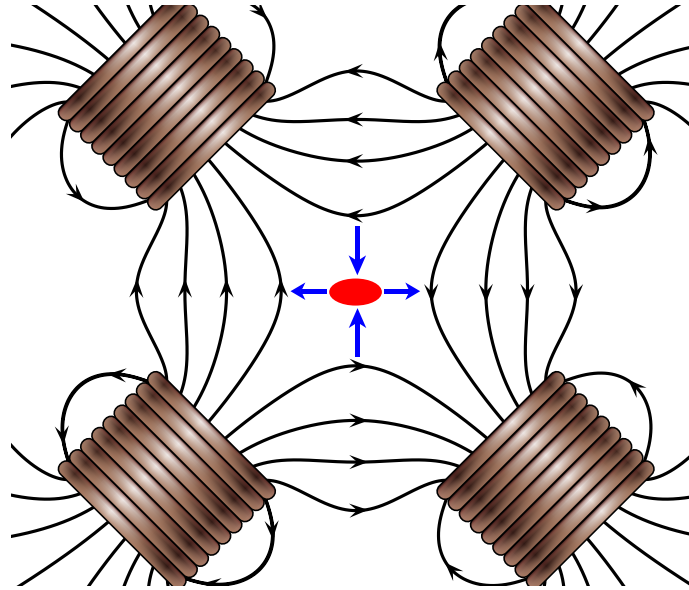


Figure 3.4: Representation of an idealised set of coil magnets in a quadrupole configuration with a proton beamspot shown as a red ellipse. The proton beam is drawn coming out of the page (*watch out!*), magnetic field lines are drawn in black and the forces acting on each bunch of protons are drawn as blue arrows.

known as the luminosity is often used to describe how much data is available for an analysis, it is written as

$$L = \frac{1}{\sigma} \frac{dN}{dt}, \quad (3.2)$$

where σ is the cross-section, a volume within which particles must pass by one another in order to interact, and N is the number of events recorded in a period of time t . For luminosity at the LHC N can be expressed as

$$N = n_{bp} n_1 n_2 \nu_r, \quad (3.3)$$

where n_{bp} is the number of colliding bunch pairs, n_1 and n_2 are the number of protons in each beam and ν_r is the frequency with which the beams rotate around the LHC's circumference. The number of particles in the beams is limited by space charge. The number of bunches is limited by the frequency that the radio-frequency cavities can operate at. The revolution frequency is limited by the strength of the dipole magnets and the circumference of the accelerator ring. Increasing luminosity by reducing the cross-section amounts to reducing the beam widths which is limited by the emittance of the beam. The LHC has already exceeded its design luminosity

providing physicists with more data to analyse than expected and plans are well underway for the upgrade to a High-Luminosity LHC (HL-LHC) [61].

3.2 The ATLAS Detector

The ATLAS detector [62] resides at a location on the LHC ring called Point 1, its full name is A Toroidal LHC ApparatuS. A diagram of the detector is shown in figure 3.5. ATLAS is considered to be a general purpose particle detector and has a wide physics program including: Higgs boson physics, top quark physics, searches for Supersymmetry and exotic states, probes of CP violation in b-quarks and light states and heavy ion physics. The detector itself is very large in size, spanning a width of 25 m and a length of 44 m and weighs 7000 tonnes which is comparable to the weight of the wrought iron content of the Eiffel tower [63].

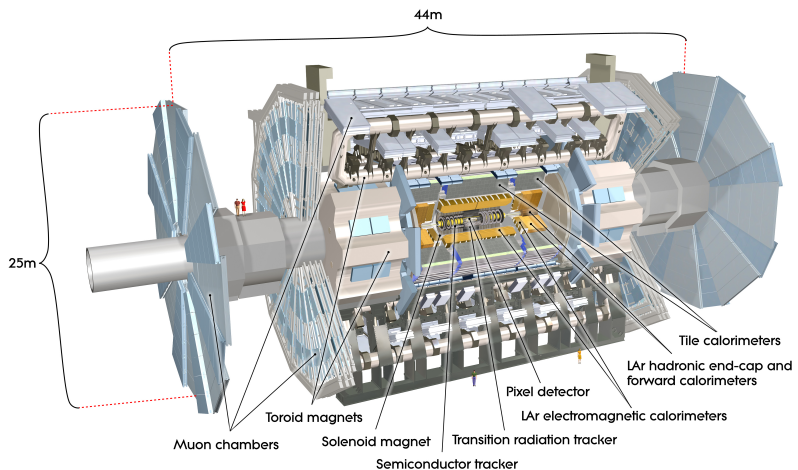


Figure 3.5: Computer generated image of the whole ATLAS detector with the major sub detectors labeled [64].

Due to the composite nature of the proton, the decay products of collisions are extremely numerous. Additionally when two bunches of protons cross there is the chance that more than one hard scattering event occurs and softer glancing collisions are also a possibility. The number of hard scattering events in a given bunch crossing is known as the pile-up of the collision and is often denoted with the symbol μ . As can be seen by inspecting equations 3.3 and 3.2 increasing the luminosity will often

cause a higher pile-up environment in the detector. The variety of decay products of each collision necessitate the use of specialised sub-detectors in order to accurately measure the output of collisions. There are dedicated sub-systems in ATLAS with the purpose of measuring properties of specific classes of particles. Ultimately in all cases a digital electrical signal is the desired output of a sub-detector which usually originates as an analogue signal. It is interesting to note that despite the many charges that are associated with the forces of nature discussed in chapter 2 the only one that we can directly measure is electric charge.

The ATLAS sub-systems are located in either the barrel of the detector or one of the end-caps. These two areas have a different geometry, and due to their relative positions with respect to the beam-pipe are exposed to different amounts of radiation, so the design of a sub-system in the barrel will differ from that of a sub-system measuring the same quantities in the end-cap. The details that follow are based on the ATLAS technical design report volumes [65, 66] unless another citation is present. Before detailing individual components it is important to detail certain properties of the detector relevant to all sub-systems. The coordinate system used to describe the ATLAS detector is known as right-handed. Three orthogonal axes (x, y, z) are used to describe the 3D space of the detector. The x-axis points towards the centre of the LHC ring, the y-axis points upwards and the z-axis points along the LHC beam pipe y-axis. The three axes meet at the interaction point which is the nominal position where bunches cross, located in the centre of the detector. Cylindrical coordinates (r, ϕ) are also often used to describe the physical features of the detector and phenomena caused by interactions in the detector that shall be referred to as analysis objects. Their definitions are that ϕ is the azimuthal angle in the x-y plane (transverse) around the beam pipe and r is the distance from the interaction point. A relativistic invariant analogy to the zenith angle of an object measured from the z-axis is pseudo-rapidity $\eta = -\ln(\tan(\theta/2))$ where θ is the ordinary zenith angle measured from the same axis.

By inspecting equation 3.1 it is clear that neutral particles for which $q = 0$ do not experience the Lorentz force. However for charged particles, as previously discussed,

a magnetic field alters the trajectory of the particle whilst preserving its energy. A large portion of the ATLAS detector is immersed in magnetic fields created by the magnet systems, and so this deflection phenomenon is present and exploited when making measurements of charged particles. There are four magnet systems in ATLAS the solenoid, the barrel toroid, and two end-cap toroids. The solenoid surrounds the inner detector whilst the toroid systems surround the muon chambers. Figure 3.6 shows a heat map of the magnetic field strengths within ATLAS, the image is from an article detailing the superconducting magnet system [67]. The magnet systems store a total energy of 1.6 GJ and produce fields of a combined volume of approximately $12 \times 10^4 \text{ m}^3$.

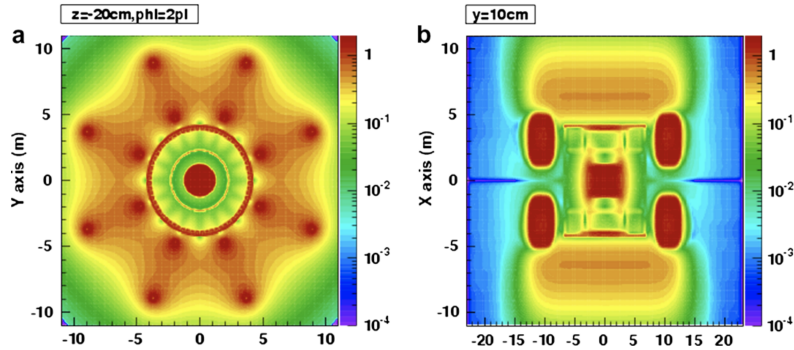


Figure 3.6: ATLAS magnetic field profile, showing a transverse cross-section in the centre of the detector (a), and a longitudinal section (b) [67].

Tracking: The Inner Detector

The Inner Detector (ID) is comprised of a number of different tracking detector sub-systems; the pixel detectors, the semiconductor tracker (SCT) and a transition radiation tracker (TRT) as seen in figure 3.9. It covers a volume corresponding with the total ϕ angle. The pixel detectors and SCT cover the range $|\eta| < 2.5$ and the TRT covers $|\eta| < 2.0$. The job of the ID is to track the propagation of charged particles through the detector. This is achieved by measuring a sequence of hits for each charged particle that propagates through its volume. The sequence of hits describing the trajectory of a given charged particle must be disentangled from other hits in the detector, track-finding algorithms are applied to this end. Using these

tracks we can measure; the direction of the particle, the sign of the electric charge of the particle, the rate of energy loss of the particle with respect to its distance traveled and by constructing the sagitta the transverse momentum of the particle (denoted p_T). An example construction of the sagitta is shown in figure 3.7 and its relation to p_T is

$$S = \frac{qL^2B}{8p_T}, \quad (3.4)$$

where L is the distance between the first and last hits in the track, q is the charge of the particle, and B is the strength of the magnetic field, in this case the field produced by the solenoid magnet system. The system is made of a single layer

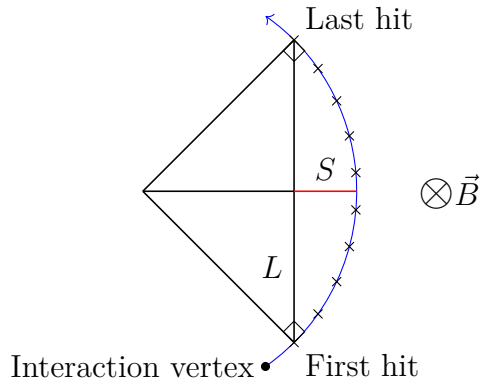


Figure 3.7: A diagram showing the geometric construction of the sagitta (S) of a track. The track is comprised of a sequence of hits marked by crosses and the “lever-arm” distance between the first and last hit in the track is marked L . Charged tracks in a magnetic field pointing into the page, as shown, form arcs of circles. The two lines marked as normal to the track are radii of the circle to which this track’s arc belongs.

coil with an inner diameter of 2.46 m and produces 2 T field in the axial direction with respect to the beam-pipe. Using multiple tracks interaction vertices can also be reconstructed, the vertex which comes from the highest energy collision in a given event is known as the primary vertex. Vertices coming from pile-up and glancing collisions of partons also need to be reconstructed in order to separate detector response due to these collisions from that of the primary vertex. So-called impact parameters d_0 and z_0 are used to identify secondary and pile-up vertices, their construction is shown in figure 3.8. These parameters are also used to perform identification of particles within the detector such as b -quarks and τ s. Tracks are

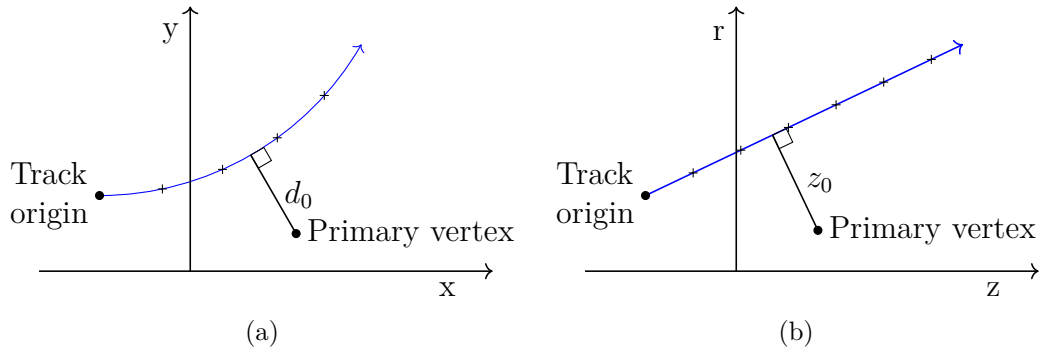


Figure 3.8: A diagram showing the geometric construction of the impact parameters d_0 and z_0 .

also used to calculate the calorimeter impact point and in general match activity in outer regions of the detector to an interaction vertex.

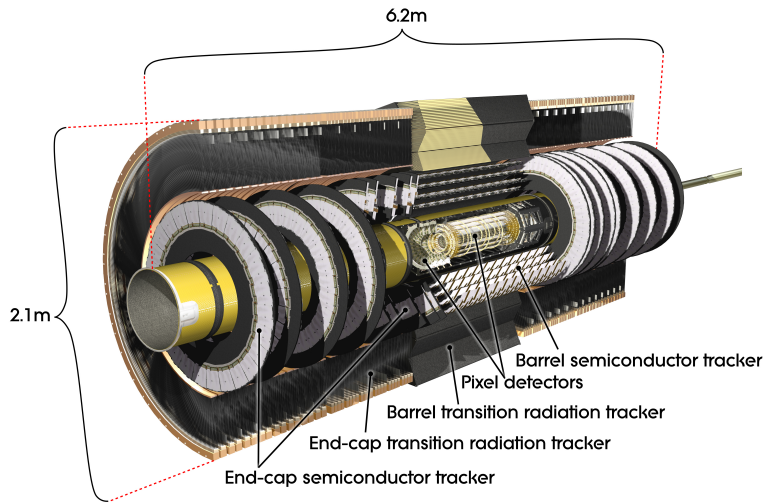


Figure 3.9: Computer generated image of the ATLAS inner detector [68].

With the exception of the TRT the tracking sub-systems are silicon based detectors. The silicon detection medium acts as a reverse bias diode. Charged particles incident on the silicon cause ionisation in the depletion layer. The products of this ionisation are electrons and holes (excess pockets of positive charge in the silicon) which produce a signal that must be handled by a read-out system. The signal is referred to as the charge collected. Application-specific integrated circuits (ASICs) are used to readout the signal performing the analogue to digital conversion. The combination of the detection medium, readout system and the printed circuit board

(PCB) on which they are joined is referred to as a module.

Pixel Detectors

There are four layers of pixel detectors that are the closest components of the ID to the beam-pipe. Pixel detectors are silicon detectors where the diodes are approximately square in shape, giving the benefit of being able to resolve hits in two directions. The design originally had three layers, each $250\ \mu\text{m}$ thick with $50\ \mu\text{m}$ by $250\ \mu\text{m}$ pixels, of oxygen doped n-type silicon crystals. During LS1 a fourth layer, closest to the beam-pipe (which was also replaced for a smaller radius version) was added. This layer is known as the insertable B-layer (IBL) [69], the motivation for its addition was to counteract degradation of original performance of the ID due to irreversible damage by radiation. As well as the inclusion of the IBL, performance degradation is mitigated by increasing the bias voltage across the pixels from 100 V (their starting voltage) to up to 600 V. Additionally the IBL being closer to the beam-pipe allows for interaction vertices to be measured more precisely. The need for better reconstruction of vertices is motivated by their role in the performance of algorithms that classify jets of activity in the detector that are initiated by B-hadrons, this is where the IBL gets its name. There are no pixel detectors in the end-caps. Each pixel is small in size which mean many can fit on one module, all requiring their own conductor for readout. The solution to this challenge is to use a complex process known as bump bonding, which is both expensive and time consuming.

Semiconductor Tracker

Next closest to the beam-pipe is the SCT whose modules have long thin strip shaped diodes. The strips provide high resolution in only a single direction. In contrast to the n-type silicon of the pixels, the strips are made from p-in-n type silicon. Each SCT module is comprised of two back to back wafers such that the orientation of the strips are offset by a small angle in order to improve coverage. Each strip is covered in a metalised layer, the strips are separated by a distance of $80\ \mu\text{m}$. A rather old

and dirty SCT module left over from the quality control testing stage of production that took place at Queen Mary University of London can be seen in figure 3.10. As can be seen in the figure the SCT modules are wire bonded to their ASICs which is cheaper and faster than the bump bonding used on the pixel modules. In order to

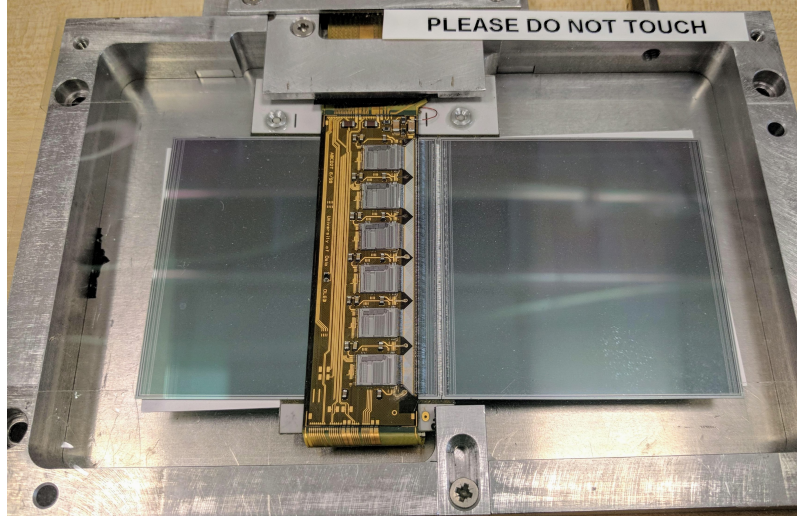


Figure 3.10: An image of an SCT long strip module mounted in a rig for testing at Queen Mary University of London.

calibrate the response of the strips a $100\text{ M}\Omega$ poly-silicon resistor is located at the end of each strip. Figure 3.11 shows an image of the snake-like structure of a poly-silicon resistor from the end of an SCT module. The modules come in two different

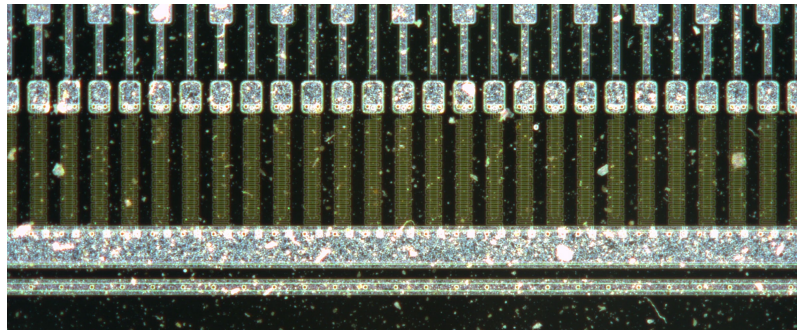


Figure 3.11: A close up image of the end of an SCT sensor in which the snake-like poly-silicon resistors are visible as a yellowish coloured structure at the end of each strip. This image was taken with a high resolution automatic area scanner commissioned by the author [70] in order to take full scans of strip sensors during the production of the ATLAS Inner Detector upgrade known as the Inner Tracker (ITk) [71, 72].

designs, short strips and long strips with the short strips forming the layer closest to the pixel detectors and the long strips on the outside. The original operating

bias voltage was 150 V but again due to radiation exposure this will raise to up to 350 V over time as necessary. There are four layers of semiconductor trackers in the barrel arranged so that sensors have a tilt with respect to a perfect coaxial cylinders of approximately 11 °. This tilt increases the amount of material that particles will travel through and is optimized to the geometry of the detector. Similarly the end-cap modules are arranged in petal like structures, with a number of different geometric designed based on the position within the end-cap.

Transition Radiation Tracker

The final layer of the ID is the TRT, the primary role of the TRT is to aid electron identification by measurement of transition radiation. The TRT is mostly made up of polyimide drift tubes with a diameter of 4 mm. The drift tubes are filled with a gas mixture whose majority constituent is xenon. These tubes operate with a voltage of -1530 V and are contained within a carbon fibre support structure. The geometric layout of the tubes is optimised individually for the barrel and end-caps.

Calorimeters

The purpose of the calorimeters is to measure the total energy of particles that pass through their volume, this is achievable only if the calorimeter stops the particle completely. A desirable side effect is that they also act as a barrier to stop particles passing through to the muon spectrometers, of course this means necessarily that muons pass through the calorimeters. There are two calorimeter systems in ATLAS the electromagnetic calorimeter (ECAL) and the hadronic calorimeter (HCAL), they will be explained in the following sections. The calorimeters are not immersed in a significant magnetic field compared to the rest of the ATLAS as seen in the heat map of figure 3.6. The geometric layout of the calorimeter systems, as well as the location of specific components can be seen in figure 3.12, in which the ID can also be seen (greyed out). Information from the two calorimeters is used in conjunction for any particles whose decay products propagate through both volumes. Both calorimeters

are split up into cells of material that are used to determine the position of decay products in the detector.

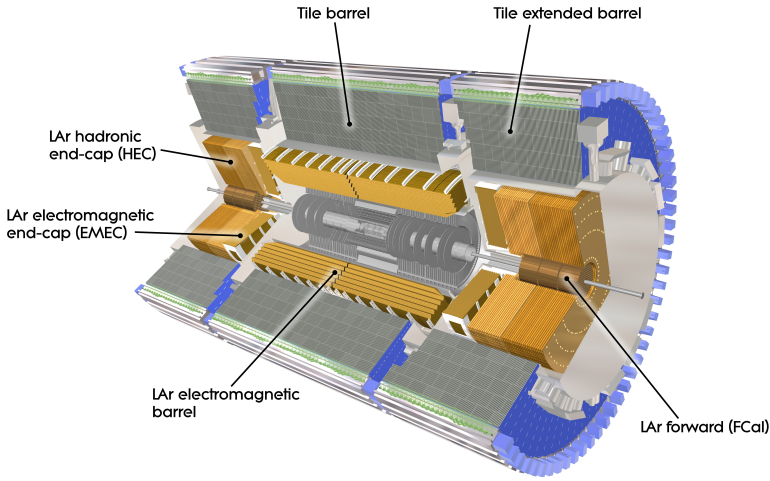


Figure 3.12: Computer Generated image of the ATLAS calorimeter [73].

High energy physics calorimeters function by measuring the shower of particles that are produced as a result of the incident particle losing its energy. Both calorimeters in ATLAS are sampling calorimeters, meaning that they are comprised of alternating layers of absorber and detection medium. The purpose of the absorber medium is to provide a material in which particle showers evolve rapidly over a short distance, though they are in general not sensitive to measuring those showers. The detection medium or active material is used to then measure those showers.

In general a good calorimeter will have the following properties. It should be hermetic meaning that there are no gaps for particles to escape through without being measured. It should have a fast response time to keep up with the rate of collisions (actually the rate of the trigger see the following section). It should be radiation tolerant in order to perform over a long period of time. It should be able to measure energy to a high resolution in order to resolve resonances over backgrounds and have a high granularity of cells in order to accurately determine the position of energy deposits (and aid particle identification). High energy resolution is greatly aided by not having anything front of the calorimeter which may change an incident particles energy before it strikes the calorimeter itself. This requirement is therefore

somewhat at odds with having a detector that has good pT resolution for electrons, positrons and photons (muons go all the way through the calorimeter anyway) due to the process by which pT is measured becoming more precise with a longer “lever-arm” distance L as seen in figure ?? and equation 3.4.

Electromagnetic Calorimeter

The ECAL is primarily concerned with measuring the energy of electrons, positrons and photons. These particles primarily interact with the electromagnetic force and so produce electromagnetic showers when they lose their energy. The ECAL resides closer to the interaction point than the HCAL and has liquid argon (LAr) as its active material. LAr is a good choice for the calorimeter which is closer to the interaction point as it is naturally resistant to damage by radiation. The absorber of the ECAL is lead, it is suitable as it has a high number of nucleons (Z) and the radiation length¹ of a given shower is inversely proportional to Z^2 . An applied electric field causes ions produced in the EM shower to drift in such a way that the signal induced is proportional to the energy deposited by the incident particle.

Hadronic Calorimeter

The HCAL end-caps use a LAr active material like the ECAL. The absorber is copper instead of lead and the dimensions are more suited to hadronic particle showers as opposed to electromagnetic. As noted before LAr is naturally radiation hard which is why it is used in the end-caps which see more radiation than the barrel regions due to almost all of the momentum of the colliding bunches of particles being in the axis of the beam-pipe. The barrel section of the hadronic calorimeter is made from scintilating tiles of active material interspersed with steel as an absorber. Scintillation is the process by which a scintillation medium produces light when energy particles travel through it. The amount of light produced is proportional to the energy of the incident particle that initiated the shower. In order to convert the

¹The radiation length X_0 is the thickness of material that reduces the energy of a particle by a factor of e the natural number.

light into a digital electrical signal photo-multiplier tubes (PMTs) are used. PMTs are able to measure very small amounts of light, even the incidence of a single photon. This is achieved by initially exploiting the photo-electric effect whereby the incident photon knocks an electron from a metallic part of the PMT. The current produced by this electron is then multiplied by a very large factor (up to 10^8 for some PMTs) by a series of dynodes (electrodes in vacuum that produce secondary emission).

Muon Spectrometers

Surrounding the calorimeters are the muon spectrometers, which form the most outer layer of the detector. Though muons are charged leptons just like electrons, their specific properties mean that dedicated muon spectrometers are required to detect them. Muons deposit far less energy per distance traveled than other particles meaning that they punch through most materials with ease. As can be seen in figure 3.13 the components of the muon spectrometers are the thin-gap chambers, cathode strip chambers, resistive plate chambers and monitor drift tubes. The barrel and end-cap toroid magnets immerse the muon spectrometers in a magnetic field which at its peak (visible in figure 3.6) has a strength of 4 T. Despite a stronger peaking magnetic field than in the solenoid observed muon tracks are often far less curved than that of their lighter cousins, the electrons. This is due to the larger mass of the muon. Muons do leave tracks in the ID and also deposit small amounts of energy in the calorimeters. Tracks in the muon spectrometers are matched up to tracks in the ID with the aid of the location of energy deposits in the calorimeters if possible. The full tracking information for muons can be used in algorithms such as overlap removal, which is used to remove muons from jets that they have been erroneously associated with by matching the muon with its ID track.

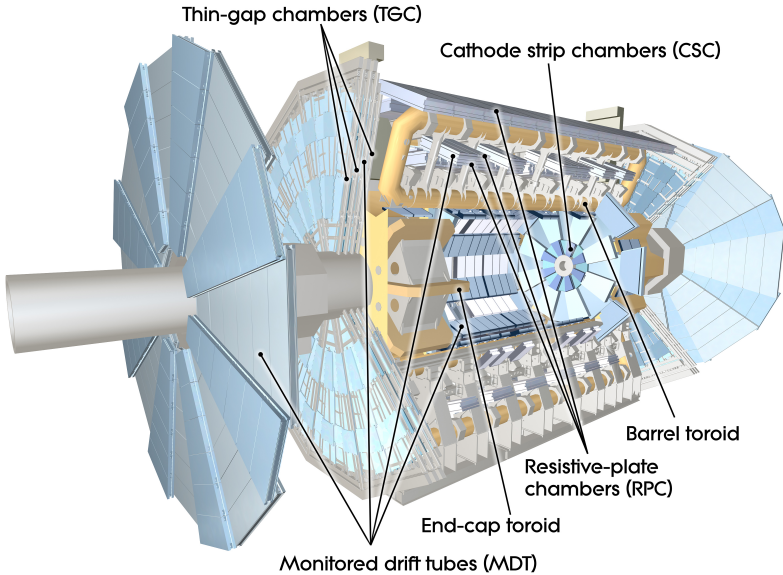


Figure 3.13: Computer generated image of the ATLAS Muons subsystem [74].

Trigger Systems

The trigger systems in ATLAS allows data to be recorded only when an event meets certain criteria. Without triggering there would be no way to decide which events to readout and which to ignore. It would be impossible to readout every interaction that occurs in the detector. The reason for this is that the geometric constraints of the detector mean that there is only a small space available for readout wires, as detection medium needs to be prioritized for sensitivity and technology limits the data rate that one can achieve through a cable of fixed area. The trigger system comes in two parts, a hardware component referred to as level one (L1) and software component referred to as the high level trigger (HLT). The L1 system is comprised of the L1 calorimeter (L1Calo) trigger which operates by searching for clusters of energy in the calorimeters and the L1 muon (L1Muon) system which coincidences in the muon systems. A third system L1 topological (L1Topo) uses regions of interest built from the L1Calo and L1Muon data which are passed to central trigger processors for selection. The various limitations of the hardware mean that these selections must be passed up to the next level of triggering, the HLT in a time window of $2.5 \mu\text{s}$. The HLT takes information from the L1 systems and uses faster versions of an offline style analysis in order to select or reject events for readout. In

order for a trigger to fire an event must pass fully all of the requirements of one of the algorithms defined by an extensive trigger menu. More information about the triggers used in the $VH(bb)$ analysis will be given in a later chapter.

Chapter 4

Machine Learning Theory

4.1 Boosted Decision Trees

Decision trees have a structure as in figure 4.1.

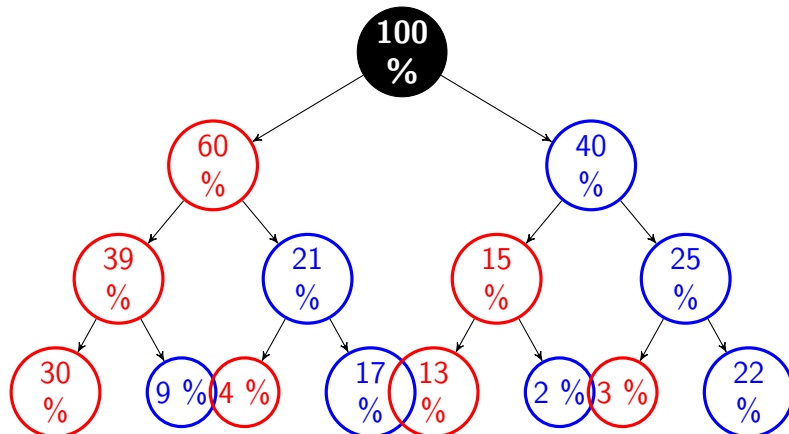


Figure 4.1: The structure of a decision tree.

4.2 Neural Networks

Neural networks have a structure as in figure 4.2.

4.3 Parametrised Neural Networks

Parametrised neural networks take extra inputs equal to the number of relevant parameters, as seen in figure 4.3.

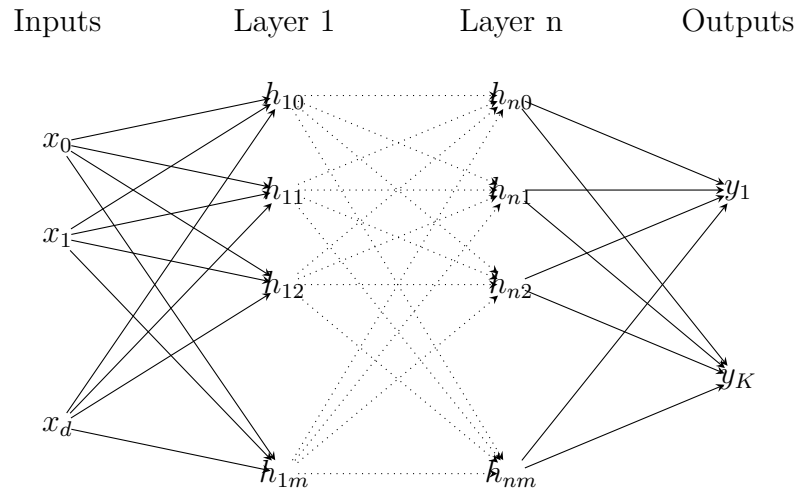


Figure 4.2: A more complex neural network containing an input layer of d nodes corresponding to data of dimensionality d , n hidden layers of m hidden units each h_{ij} (where i indexes hidden layer and j indexes a particular unit) and an output layer of K predictive units y_k .

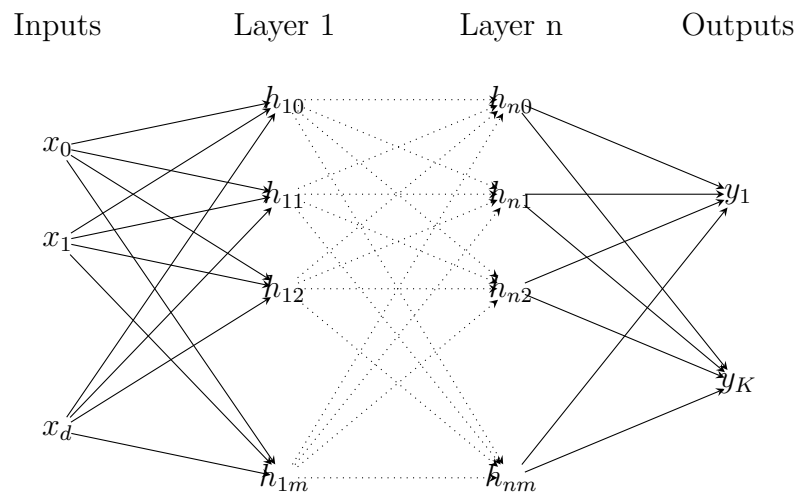


Figure 4.3: A more complex neural network containing an input layer of d nodes corresponding to data of dimensionality d , n hidden layers of m hidden units each h_{ij} (where i indexes hidden layer and j indexes a particular unit) and an output layer of K predictive units y_k .

Chapter 5

Reconstruction and Selection

5.1 Triggers

5.2 Athena and the CxAOD Framework

Data recorded by the ATLAS detector is passed through the central collaboration software framework Athena before entering the analysis level data processing.

Athena is responsible for the steps shown in figure 5.1. As can be seen in the figure Athena processes both data recorded from collisions and Monte-Carlo simulated predictions. Steps up until and including reconstruction are required to transform the raw or simulated read-out of the detector into what are known as physics objects. These physics objects correspond to UV and IR safe descriptions particles and hadron showers e.g. leptons and jets. Given the initial transverse energy of the collisions (zero) any missing transverse energy (E_{miss}^T) is also reconstructed based on the sum of the transverse energy of all objects in an event, this missing energy indicates the presence of particles in the event that cannot be detected by any of ATLAS subsystems. The only particles in the Standard Model for which this is expected are neutrinos. The files containing the reconstructed physics objects adhere to the ATLAS Event Data Model (EDM) and are referred to as Analysis Object Data (xAOD). After reconstruction a part of Athena called the derivation framework is used to produce skimmed and slimmed xAODs known as Derived xAODs

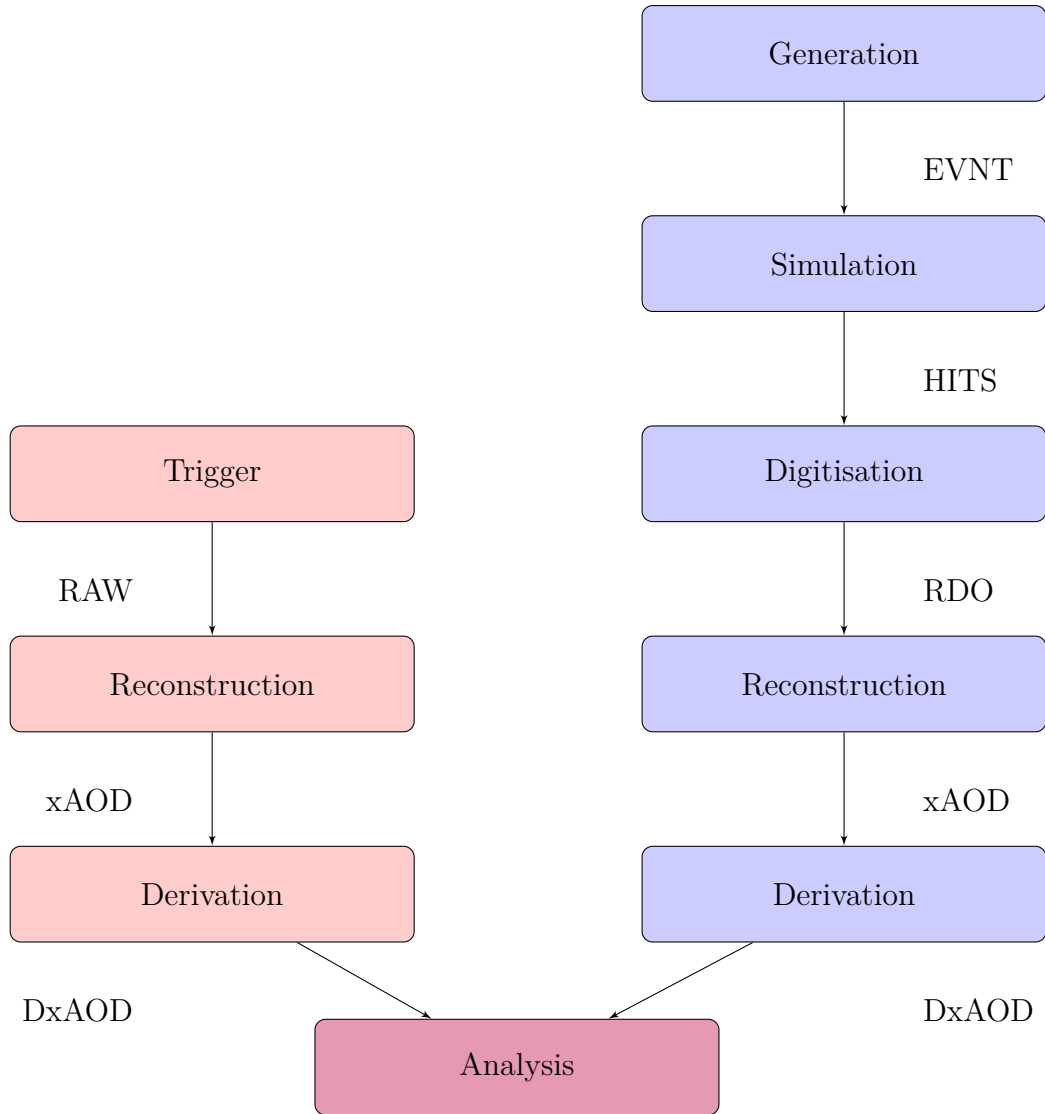


Figure 5.1: A flow chart showing the Athena data processing chain. Red nodes indicate the presence of data recorded from collisions and blue nodes indicate the presence of Monte-Carlo simulated events.

(DxAODs). The reduction of these files is carried out based on a loose selection criteria, the criteria used in the VH(bb) analysis are shown in table ??.

DxAODs are the usual starting point for analysis level software, in the case of this analysis the CxAOD Framework. Of course xAODs can also be used as the starting point for analysis they are just larger. As in figure 5.2 The CxAOD Framework has two major components the Maker and the Reader. The job of the maker is to further slim the data by performing pre-selection cuts and also to apply calibrations which will be detailed below, the output of the Maker is called a Calibrated xAOD (CxAOD). The Reader takes a CxAOD as input and performs the analysis event

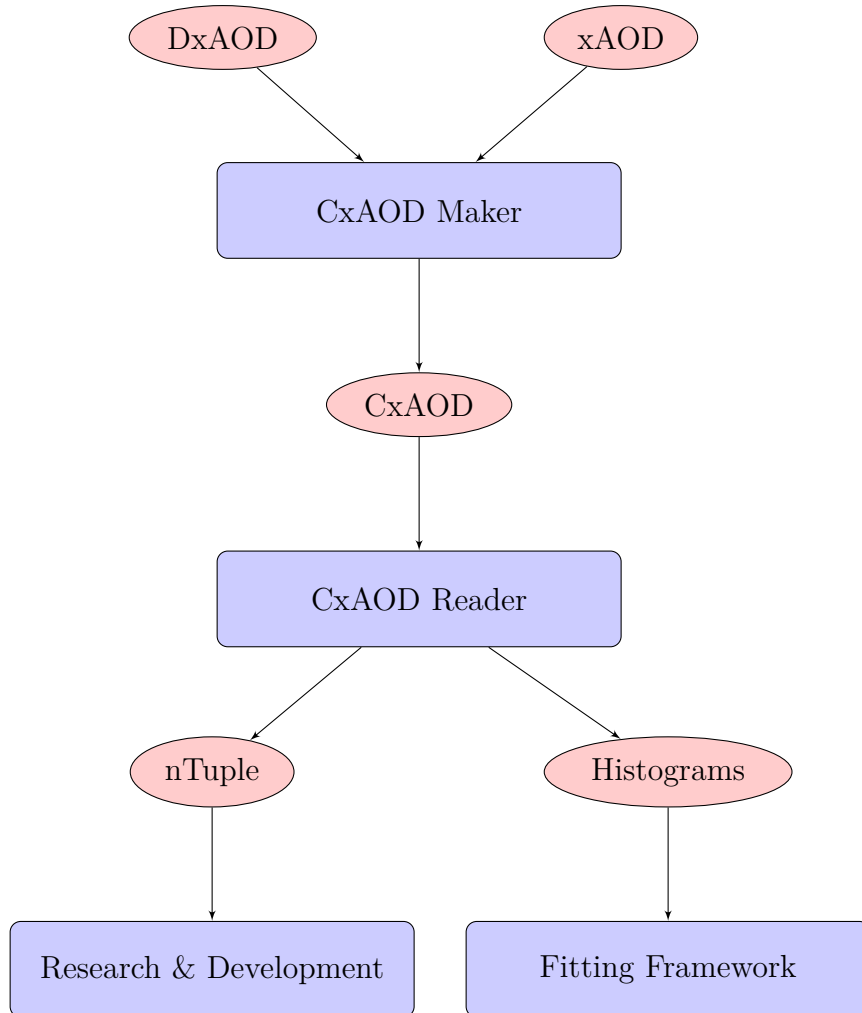


Figure 5.2: A flow chart showing the CxAOD Framework data processing chain. The red elliptical nodes indicate data formats and the blue rectangular nodes indicate software modules.

selection, it can output histograms or nTuples.

The Maker applies selections the selections of each of the three analysis channels, defined in section 5.3. CxAODs are produced separately for each of the three channels as the different background compositions and signal signatures require different optimisation. Pre-selection is performed on jets based on application of requirements on transverse momentum and pseudo-rapidity. A tool known as the Jet Vertex Tagger (JVT) is used to remove jets resulting from pileup from events.

Name	p_T	$ \eta $	ID	d_0^{sig}	$ \Delta z_0 \sin \theta $	Isolation
electrons						
VH-loose	> 7 GeV	< 2.47	LH Loose	< 5	< 0.5 mm	FCLoose
ZH-signal	> 27 GeV	< 2.47	LH Loose	< 5	< 0.5 mm	FCLoose
WH-signal	> 27 GeV	< 2.47	LH Tight	< 5	< 0.5 mm	FixedCutHighPtCaloOnly
muons						
VH-loose	> 7 GeV	< 2.7	Loose quality	< 3	< 0.5 mm	FixecdCutLoose
ZH-signal	> 27 GeV	< 2.5	Loose quality	< 3	< 0.5 mm	FixecdCutLoose
WH-signal	> 27 GeV	< 2.5	Medium quality	< 3	< 0.5 mm	FixedCutHighPtCaloOnly

Table 5.1: Definitions of the VH leptons used to define and select events for the three analysis channels where d_0^{sig} is the measured with respect to the beam line.

5.3 Channel Definitions and Lepton Selections

The channels of the VH(bb) analysis are defined by the number of observed charged leptons (e or μ) in the decay of the vector boson. There is one channel for the study of WH(bb) decays where the leptonic decay $W \rightarrow \ell\nu$ yields a single charged lepton. There are two channels for the study of ZH(bb), the zero lepton channel, $Z \rightarrow \nu\nu$, and the two lepton channel, $Z \rightarrow \ell\ell$.

Two classifications of lepton are defined in order to categorise events into the individual channels of the analysis, these are called VH-loose and VH-signal electrons, channels are kept orthogonal by requiring different numbers of both lepton categories. These classifications are defined in table 5.1.

5.4 Triggers

Trigger Name	Period	Threshold (GeV)	Description
HLT_xe70_L1XE50	2015	70 GeV	Seeded using the level L1_XE50
HLT_xe90_mht_L1XE50	2016 (A-D3)	90 GeV	(L1_XE55) LAr and Tile calorimeter triggers, calibrated at the EM
HLT_xe110_mht_L1XE50	2016 ($\geq D4$)	110 GeV	scale, with a threshold of 50(55) GeV.
HLT_xe110_pufit_L1XE55	2017	110 GeV	
HLT_xe110_pufit_xe70_L1XE50	2018	110 GeV	

Table 5.2: MET triggers used during the 2015, 2016, 2017 and 2018 data collection period [?].

Trigger Name	Period	Threshold (GeV)	Description
HLT_e24_lhmedium_L1EM20VH	2015	24 GeV	Seeded using L1EM20VH level 1 trigger calibrated at the EM scale with a threshold of 20 GeV, and require medium ID quality.
HLT_e60_lhmedium	2015	60 GeV	Seeded using L1EM20VH level 1 trigger calibrated at the EM scale with a threshold of 20 GeV, and require medium ID quality.
HLT_e120_lhloose	2015	120 GeV	Seeded using L1EM20VH level 1 trigger calibrated at the EM scale with a threshold of 20 GeV, and require loose ID quality.
HLT_e26_lhtight_nod0_ivarloose	2016 – 2018	26 GeV	Tight likelihood ID required, and variable loose isolation required
HLT_e60_lhmedium(_nod0)	2016 – 2018	60 GeV	Medium ID likelihood required
HLT_e140_lhloose(_nod0)	2016 – 2018	140 GeV	Loose ID likelihood required
HLT_e300_etcut	2018	300 GeV	No ID requirements.

Table 5.3: Single Electron triggers used during the 2015-2018 data collection period [?]. Please note that the notation, (A, D3, ...) refer ATLAS collection periods in 2016.

Trigger Name	Period	Threshold (GeV)	Description
HLT_mu20_iloose_L1MU15	2015	20 GeV	Seeded using L1MU15 level 1 trigger with a threshold of 15 GeV, and requiring loose isolation requirements.
HLT_mu50	2015 – 2018	60 GeV	No isolation requirements.
HLT_mu26_ivarmedium	2016 – 2018	26 GeV	Variable cone medium isolation requirements

Table 5.4: Single muon triggers used during the 2015-2018 data collection period [?].

5.5 Jets

5.6 Overlap Removal

5.7 Missing Transverse Momentum

5.8 Categorisation into Analysis Regions

Top $e\mu$ control region

$\Delta R(b, b)$ Control Regions

Chapter 6

Fit Models

6.1 Profile Likelihood Fits

6.2 VH(b,b) multi-variate discriminant fit

6.3 Di-jet mass fit

6.4 VZ Cross-check fit

Variation	Values	
Sherpa 2.2.1		
Factorisation scale (μ_F)	$2\mu_F$	$0.5\mu_F$
Renormalisation scale (μ_R)	$2\mu_R$	$0.5\mu_R$
PDF Variation	MMHT2014nnlo68cl	CT14nnlo
Sherpa 2.1		
Re-summation scale (μ_S)	$2\mu_S$	$0.5\mu_S$
CKKW Merging scale	15 GeV	30 GeV

Table 7.1: A summary of the Sherpa 2.2.1 and Sherpa 2.1 internal variations that are used to model V + jets processes.

Chapter 7

Background Modelling

7.1 Novel Modelling Techniques

Multi-dimensional re-weighting

Inferring missing information with parametrised neural networks

7.2 2 lepton channel $Z + \text{jets}$ modelling

Extrapolation to 0 lepton channel

7.3 Modelling of other backgrounds

Chapter 8

Results

**8.1 VH(b,b) multi-variate discriminant fit
results**

8.2 Di-jet mass fit results

8.3 VZ Cross-check results

Chapter 9

Conclusion

9.1 Future studies

q

Bibliography

- [1] Georges Aad et al. (ATLAS Collaboration). Observation of a new particle in the search for the Standard Model Higgs boson with the ATLAS detector at the LHC. *Phys. Lett.*, B716:1–29, 2012. doi: 10.1016/j.physletb.2012.08.020.
- [2] Serguei Chatrchyan et al. (CMS Collaboration). Observation of a new boson at a mass of 125 GeV with the CMS experiment at the LHC. *Phys. Lett.*, B716:30–61, 2012. doi: 10.1016/j.physletb.2012.08.021.
- [3] Will J. Percival, Shaun Cole, Daniel J. Eisenstein, Robert C. Nichol, John A. Peacock, Adrian C. Pope, and Alexander S. Szalay. Measuring the baryon acoustic oscillation scale using the Sloan Digital Sky Survey and 2df Galaxy Redshift Survey. *Monthly Notices of the Royal Astronomical Society*, 381(3):1053–1066, 2007. doi: 10.1111/j.1365-2966.2007.12268.x. URL <http://dx.doi.org/10.1111/j.1365-2966.2007.12268.x>.
- [4] Fabio Iocco, Gianpiero Mangano, Gennaro Miele, Ofelia Pisanti, and Pasquale D. Serpico. Primordial Nucleosynthesis: from precision cosmology to fundamental physics. *Phys. Rept.*, 472:1–76, 2009. doi: 10.1016/j.physrep.2009.02.002.
- [5] M. Kowalski et al. Improved Cosmological Constraints from New, Old and Combined Supernova Datasets. *Astrophys. J.*, 686:749–778, 2008. doi: 10.1086/589937.
- [6] Richard Massey et al. Dark matter maps reveal cosmic scaffolding. *Nature*, 445:286, 2007. doi: 10.1038/nature05497.

- [7] Douglas Clowe, Marusa Bradac, Anthony H. Gonzalez, Maxim Markevitch, Scott W. Randall, Christine Jones, and Dennis Zaritsky. A direct empirical proof of the existence of dark matter. *Astrophys. J.*, 648:L109–L113, 2006. doi: 10.1086/508162.
- [8] J. Anthony Tyson, Greg P. Kochanski, and Ian P. Dell’Antonio. Detailed mass map of CL0024+1654 from strong lensing. *Astrophys. J.*, 498:L107, 1998. doi: 10.1086/311314.
- [9] Lars Bergstrom. Dark Matter Candidates. *New J. Phys.*, 11:105006, 2009. doi: 10.1088/1367-2630/11/10/105006.
- [10] C. Patrignani et al. Review of Particle Physics. *Chin. Phys.*, C40(10):100001, 2016. doi: 10.1088/1674-1137/40/10/100001.
- [11] F. Zwicky. Republication of: The redshift of extragalactic nebulae. *General Relativity and Gravitation*, 41:207–224, January 2009. doi: 10.1007/s10714-008-0707-4.
- [12] Lars Bergström. Nonbaryonic dark matter: Observational evidence and detection methods. *Rept. Prog. Phys.*, 63:793, 2000. doi: 10.1088/0034-4885/63/5/2r3.
- [13] Gianfranco Bertone, Dan Hooper, and Joseph Silk. Particle dark matter: Evidence, candidates and constraints. *Phys. Rept.*, 405:279–390, 2005. doi: 10.1016/j.physrep.2004.08.031.
- [14] Roel Aaij et al. Measurement of the ratio of branching fractions $\mathcal{B}(\bar{B}^0 \rightarrow D^{*+}\tau^-\bar{\nu}_\tau)/\mathcal{B}(\bar{B}^0 \rightarrow D^{*+}\mu^-\bar{\nu}_\mu)$. *Phys. Rev. Lett.*, 115(11):111803, 2015. doi: 10.1103/PhysRevLett.115.159901, 10.1103/PhysRevLett.115.111803. [Erratum: *Phys. Rev. Lett.* 115,no.15,159901(2015)].
- [15] J. P. Lees et al. Evidence for an excess of $\bar{B} \rightarrow D^{(*)}\tau^-\bar{\nu}_\tau$ decays. *Phys. Rev. Lett.*, 109:101802, 2012. doi: 10.1103/PhysRevLett.109.101802.

- [16] Thomas Blum, Achim Denig, Ivan Logashenko, Eduardo de Rafael, B. Lee Roberts, Thomas Teubner, and Graziano Venanzoni. The Muon ($g-2$) Theory Value: Present and Future. 2013.
- [17] Carl E. Carlson. The Proton Radius Puzzle. *Prog. Part. Nucl. Phys.*, 82:59–77, 2015. doi: 10.1016/j.ppnp.2015.01.002.
- [18] Bernat Capdevila, Andreas Crivellin, Sébastien Descotes-Genon, Joaquim Matias, and Javier Virto. Patterns of New Physics in $b \rightarrow s\ell^+\ell^-$ transitions in the light of recent data. *JHEP*, 01:093, 2018. doi: 10.1007/JHEP01(2018)093.
- [19] John D. Hobbs, Mark S. Neubauer, and Scott Willenbrock. Tests of the standard electroweak model at the energy frontier. *Rev. Mod. Phys.*, 84:1477–1526, Oct 2012. doi: 10.1103/RevModPhys.84.1477. URL <https://link.aps.org/doi/10.1103/RevModPhys.84.1477>.
- [20] L. Nodulman. Experimental tests of the standard model. *NATO Sci. Ser. C*, 534:147–193, 1999. doi: 10.1007/978-94-011-4689-0_4.
- [21] Morad Aaboud et al. Observation of $H \rightarrow b\bar{b}$ decays and VH production with the ATLAS detector. *Phys. Lett.*, B786:59–86, 2018. doi: 10.1016/j.physletb.2018.09.013.
- [22] Francis Halzen, Alan D. Martin, and Nilotpal Mitra. Quarks and leptons: An introductory course in modern particle physics. *American Journal of Physics*, 53(3):287–287, 1985. doi: 10.1119/1.14146. URL <https://doi.org/10.1119/1.14146>.
- [23] Mark Thomson. *Modern Particle Physics*. Cambridge University Press, 2013. doi: 10.1017/CBO9781139525367.
- [24] A. Zannoni. On the Quantization of the Monoatomic Ideal Gas. *eprint arXiv:cond-mat/9912229*, December 1999.
- [25] On the theory of quantum mechanics. *Proceedings of the Royal Society of London A: Mathematical, Physical and Engineering Sciences*, 112(762):

- 661–677, 1926. ISSN 0950-1207. doi: 10.1098/rspa.1926.0133. URL <http://rspa.royalsocietypublishing.org/content/112/762/661>.
- [26] A. Borrelli. *Compendium of Quantum Physics*. 2009.
- [27] Emmy Noether. Invariant variation problems. *Transport Theory and Statistical Physics*, 1(3):186–207, Jan 1971. ISSN 1532-2424. doi: 10.1080/00411457108231446. URL <http://dx.doi.org/10.1080/00411457108231446>.
- [28] Albert Einstein. On the electrodynamics of moving bodies. *Annalen Phys.*, 17: 891–921, 1905. doi: 10.1002/andp.200590006. [Annalen Phys.14,194(2005)].
- [29] V. Alan Kostelecký and Neil Russell. Data tables for lorentz and *cpt* violation. *Rev. Mod. Phys.*, 83:11–31, Mar 2011. doi: 10.1103/RevModPhys.83.11. URL <https://link.aps.org/doi/10.1103/RevModPhys.83.11>.
- [30] David Mattingly. Modern tests of lorentz invariance. *Living Reviews in Relativity*, 8(1):5, Sep 2005. ISSN 1433-8351. doi: 10.12942/lrr-2005-5. URL <https://doi.org/10.12942/lrr-2005-5>.
- [31] S Liberati. Tests of lorentz invariance: a 2013 update. *Classical and Quantum Gravity*, 30(13):133001, jun 2013. doi: 10.1088/0264-9381/30/13/133001. URL <https://doi.org/10.1088%2F0264-9381%2F30%2F13%2F133001>.
- [32] Clifford M. Will Mark P. Haugan. Modern tests of special relativity. *Physics Today*, 40(5):69, 1987. doi: 10.1063/1.881074. URL <https://doi.org/10.1063/1.881074>.
- [33] Floyd W. Stecker. Limiting superluminal electron and neutrino velocities using the 2010 crab nebula flare and the icecube pev neutrino events. *Astroparticle Physics*, 56:16 – 18, 2014. ISSN 0927-6505. doi: <https://doi.org/10.1016/j.astropartphys.2014.02.007>. URL <http://www.sciencedirect.com/science/article/pii/S092765051400019X>.

- [34] R. Abbasi et al. Search for a lorentz-violating sidereal signal with atmospheric neutrinos in icecube. *Phys. Rev. D*, 82:112003, Dec 2010. doi: 10.1103/PhysRevD.82.112003. URL <https://link.aps.org/doi/10.1103/PhysRevD.82.112003>.
- [35] Enrico Borriello, Sovan Chakraborty, Alessandro Mirizzi, and Pasquale Dario Serpico. Stringent constraint on neutrino lorentz invariance violation from the two icecube pev neutrinos. *Phys. Rev. D*, 87:116009, Jun 2013. doi: 10.1103/PhysRevD.87.116009. URL <https://link.aps.org/doi/10.1103/PhysRevD.87.116009>.
- [36] E. Schrödinger. An undulatory theory of the mechanics of atoms and molecules. *Phys. Rev.*, 28:1049–1070, Dec 1926. doi: 10.1103/PhysRev.28.1049. URL <https://link.aps.org/doi/10.1103/PhysRev.28.1049>.
- [37] Sheldon L. Glashow. The renormalizability of vector meson interactions. *Nucl. Phys.*, 10:107–117, 1959. doi: 10.1016/0029-5582(59)90196-8.
- [38] Abdus Salam and John Clive Ward. Weak and electromagnetic interactions. *Nuovo Cim.*, 11:568–577, 1959. doi: 10.1007/BF02726525.
- [39] Steven Weinberg. A Model of Leptons. *Phys. Rev. Lett.*, 19:1264–1266, 1967. doi: 10.1103/PhysRevLett.19.1264.
- [40] C. S. Wu, E. Ambler, R. W. Hayward, D. D. Hoppes, and R. P. Hudson. Experimental test of parity conservation in beta decay. *Phys. Rev.*, 105:1413–1415, Feb 1957. doi: 10.1103/PhysRev.105.1413. URL <https://link.aps.org/doi/10.1103/PhysRev.105.1413>.
- [41] G. Arnison et al. Experimental Observation of Isolated Large Transverse Energy Electrons with Associated Missing Energy at $s^{**}(1/2) = 540\text{-GeV}$. *Phys. Lett.*, B122:103–116, 1983. doi: 10.1016/0370-2693(83)91177-2. [,611(1983)].
- [42] M. Banner et al. Observation of Single Isolated Electrons of High Transverse Momentum in Events with Missing Transverse Energy at the CERN anti-p p

- Collider. *Phys. Lett.*, B122:476–485, 1983. doi: 10.1016/0370-2693(83)91605-2. [,7.45(1983)].
- [43] G. Arnison et al. Experimental Observation of Lepton Pairs of Invariant Mass Around 95-GeV/c**2 at the CERN SPS Collider. *Phys. Lett.*, B126:398–410, 1983. doi: 10.1016/0370-2693(83)90188-0. [,7.55(1983)].
- [44] P. Bagnaia et al. Evidence for $Z_0 \rightarrow e^+ e^-$ at the CERN anti-p p Col- linder. *Phys. Lett.*, B129:130–140, 1983. doi: 10.1016/0370-2693(83)90744-X. [,7.69(1983)].
- [45] F. Englert and R. Brout. Broken symmetry and the mass of gauge vector mesons. *Phys. Rev. Lett.*, 13:321–323, Aug 1964. doi: 10.1103/PhysRevLett. 13.321. URL <https://link.aps.org/doi/10.1103/PhysRevLett.13.321>.
- [46] Peter W. Higgs. Broken symmetries and the masses of gauge bosons. *Phys. Rev. Lett.*, 13:508–509, Oct 1964. doi: 10.1103/PhysRevLett.13.508. URL <https://link.aps.org/doi/10.1103/PhysRevLett.13.508>.
- [47] G. S. Guralnik, C. R. Hagen, and T. W. B. Kibble. Global conservation laws and massless particles. *Phys. Rev. Lett.*, 13:585–587, Nov 1964. doi: 10.1103/PhysRevLett.13.585. URL <https://link.aps.org/doi/10.1103/PhysRevLett.13.585>.
- [48] P. W. Anderson. Plasmons, gauge invariance, and mass. *Phys. Rev.*, 130: 439–442, Apr 1963. doi: 10.1103/PhysRev.130.439. URL <https://link.aps.org/doi/10.1103/PhysRev.130.439>.
- [49] D. de Florian et al. Handbook of LHC Higgs Cross Sections: 4. Deciphering the Nature of the Higgs Sector. 2016. doi: 10.23731/CYRM-2017-002.
- [50] Oliver Sim Brüning, Paul Collier, P Lebrun, Stephen Myers, Ranko Ostojic, John Poole, and Paul Proudlock. *LHC Design Report*. CERN Yellow Reports: Monographs. CERN, Geneva, 2004. URL <https://cds.cern.ch/record/782076>.

- [51] *LEP design report.* CERN, Geneva, 1984. URL <https://cds.cern.ch/record/102083>. Copies shelved as reports in LEP, PS and SPS libraries.
- [52] CERN. ATLAS: Letter of intent for a general purpose p p experiment at the large hadron collider at CERN. 1992.
- [53] M. Della Negra et al. CMS: letter of intent by the CMS Collaboration for a general purpose detector at LHC. Technical Report CERN-LHCC-92-003. LHCC-I-1, CERN, Geneva, 1992. URL <https://cds.cern.ch/record/290808>. Open presentation to the LHCC 5 November 1992, M. Della Negra/CERN, CMS Spokesman.
- [54] H. Dijkstra, Hans Jürgen Hilke, Tatsuya Nakada, and Thomas Ypsilantis. LHCb Letter of Intent, LHCb Collaboration. 1995.
- [55] Letter of Intent for A Large Ion Collider Experiment [ALICE]. Technical Report CERN-LHCC-93-016. LHCC-I-4, CERN, Geneva, 1993. URL <https://cds.cern.ch/record/290825>.
- [56] G Giacomelli, A A Faust, and James L Pinfold. A search for highly ionizing particles and slow exotic decays at the LHC using the MOEDAL detectors: letter of intent. Technical Report CERN-LHCC-98-05. LHCC-I-19, CERN, Geneva, Feb 1998. URL <https://cds.cern.ch/record/347906>.
- [57] W Kienzle, , et al. *Total cross section: elastic scattering and diffraction dissociation at the LHC.* Letter of Intent. CERN, Geneva, 1997. URL <http://cds.cern.ch/record/335255>.
- [58] O Adriani. LHCf Letter of Intent for a p-Pb run. A precise study of forward physics in $\sqrt{s_{NN}} = 4.4$ TeV proton-Lead ion collisions with LHCf at the LHC. Technical Report CERN-LHCC-2011-015. LHCC-I-021, CERN, Geneva, Dec 2011. URL <https://cds.cern.ch/record/1404163>.
- [59] Christiane Lefèvre. The CERN accelerator complex. Complexe des accélérateurs du CERN. Dec 2008. URL <https://cds.cern.ch/record/1260465>.

- [60] Design Report Tevatron 1 project. Technical Report FERMILAB-DESIGN-1984-01, 1984. URL <https://cds.cern.ch/record/1478620>.
- [61] I. Bejar Alonso and L. Rossi. HiLumi LHC Technical Design Report. 2015.
- [62] Georges Aad et al. (ATLAS Collaboration). The atlas experiment at the cern large hadron collider. *Journal of Instrumentation*, 3(08):S08003, 2008. URL <http://stacks.iop.org/1748-0221/3/i=08/a=S08003>.
- [63] David Hanser. *Architecture of France*. Greenwood Press, Westport, Conn, 2006. ISBN 978-0-313-31902-0.
- [64] Joao Pequenao. Computer generated image of the whole ATLAS detector. Mar 2008. URL <https://cds.cern.ch/record/1095924>.
- [65] A. Airapetian et al. ATLAS: Detector and physics performance technical design report. Volume 1. 1999.
- [66] A. Airapetian et al. ATLAS: Detector and physics performance technical design report. Volume 2. 1999.
- [67] H.H.J. ten Kate. The atlas superconducting magnet system at the large hadron collider. *Physica C: Superconductivity*, 468(15):2137 – 2142, 2008. ISSN 0921-4534. doi: <https://doi.org/10.1016/j.physc.2008.05.146>. URL <http://www.sciencedirect.com/science/article/pii/S0921453408004541>. Proceedings of the 20th International Symposium on Superconductivity (ISS 2007).
- [68] Joao Pequenao. Computer generated image of the ATLAS inner detector. Mar 2008. URL <https://cds.cern.ch/record/1095926>.
- [69] M Capeans, G Darbo, K Einsweiller, M Elsing, T Flick, M Garcia-Sciveres, C Gemme, H Pernegger, O Rohne, and R Vuillermet. ATLAS Insertable B-Layer Technical Design Report. Technical Report CERN-LHCC-2010-013. ATLAS-TDR-19, Sep 2010. URL <https://cds.cern.ch/record/1291633>.

- [70] Thomas Paul Charman, Bart Hommels, and Adrian John Bevan. Authorship Qualification Task: ATLAS ITk Sensor Scanner Documentation (QMUL). Technical Report ATL-COM-ITK-2019-018, CERN, Geneva, Jan 2019. URL <https://cds.cern.ch/record/2674404>.
- [71] Ben Brueers. The design and layout of the Phase-II upgrade of the Inner tracker of the ATLAS experiment. Jul 2019. URL <https://cds.cern.ch/record/2681301>.
- [72] John Stakely Keller. The ATLAS ITk Strip Detector System for the Phase-II LHC Upgrade. Feb 2019. URL <https://cds.cern.ch/record/2663172>.
- [73] Joao Pequenao. Computer Generated image of the ATLAS calorimeter. Mar 2008. URL <https://cds.cern.ch/record/1095927>.
- [74] Joao Pequenao. Computer generated image of the ATLAS Muons subsystem. Mar 2008. URL <https://cds.cern.ch/record/1095929>.